Paleoceanography and Paleoclimatology

RESEARCH ARTICLE
10.1029/2021PA004266

Key Points:

- Clumped isotopes reveal changes in temperature and water isotopes over the past 36,000 years consistent with transient model simulations
- Warming since the LGM was 16.4 ± 2.6°C, 2.5–3x the global average, likely due to proximity of site to ice margin
- Model analysis indicates $\delta^{18}O$ depletion in this location at the LGM is largely a result of the North American ice sheets

Supporting Information:

Supporting Information may be found in the online version of this article.

Correspondence to:

R. Lopez-Maldonado and A. Tripati,
ricardolopez9080@gmail.com;
atripati@g.ucla.edu

Citation:

Lopez-Maldonado, R., Bateman, J. B., Ellis, A., Bader, N. E., Ramirez, P., Arnold, A., et al. (2023). Paleoclimate changes in the Pacific Northwest over the past 36,000 years from clumped isotope measurements and model analysis. *Paleoceanography and Paleoclimatology*, *38*, e2021PA004266. https://doi.org/10.1029/2021PA004266

Received 5 APR 2021
Accepted 4 NOV 2022

Author Contributions:

Conceptualization: Ricardo Lopez-Maldonado, Andre Ellis, Nicholas E. Bader, Pedro Ramirez, Osinachi Ajoku, Hung-I Lee, Gregory Jesmok, Clay Tabor
Formal analysis: Ricardo Lopez-Maldonado, Pedro Ramirez, Alexandrea Arnold, Osinachi Ajoku, Hung-I Lee, Gregory Jesmok, Deepshikha Upadhyay, Bryce Mitsunaga, Ben Elliott, Clay Tabor, Aradhna Tripati

Paleoclimate Changes in the Pacific Northwest Over the Past 36,000 Years From Clumped Isotope Measurements and Model Analysis

Ricardo Lopez-Maldonado[1,2], Jesse Bloom Bateman[2,3], Andre Ellis[1], Nicholas E. Bader[4], Pedro Ramirez[1], Alexandrea Arnold[2], Osinachi Ajoku[5,6], Hung-I Lee[2,7], Gregory Jesmok[2,8], Deepshikha Upadhyay[2], Bryce Mitsunaga[2,9], Ben Elliott[2], Clay Tabor[10], and Aradhna Tripati[2,11]

[1]Department of Geoscience and Environment, California State University, Los Angeles, CA, USA, [2]Department of Atmospheric and Oceanic Sciences, Department of Earth, Planetary, and Space Sciences, Center for Diverse Leadership in Science, American Indian Studies Center, Institute of the Environment and Sustainability, University of California, Los Angeles, Los Angeles, CA, USA, [3]Department of Biology, SUNY Cortland, Cortland, NY, USA, [4]Department of Geology, Whitman College, Walla Walla, WA, USA, [5]Department of Interdisciplinary Studies, Howard University, Washington, DC, USA, [6]National Center for Atmospheric Research, Boulder, CO, USA, [7]Department of Geophysical Sciences, University of Chicago, Chicago, IL, USA, [8]Department of Geology, California State University, Northridge, CA, USA, [9]Department of Geology, Brown University, Providence, RI, USA, [10]Department of Geosciences, University of Connecticut, Storrs, CT, USA, [11]UMR6538 Géosciences Océan, Institut Universitaire Européen de la Mer, Plouzané, France

Abstract Since the last glacial period, North America has experienced dramatic changes in regional climate, including the collapse of ice sheets and changes in precipitation. We use clumped isotope (Δ_{47}) thermometry and carbonate $\delta^{18}O$ measurements of glacial and deglacial pedogenic carbonates from the Palouse Loess to provide constraints on hydroclimate changes in the Pacific Northwest. We also employ analysis of climate model simulations to help us further provide constraints on the hydroclimate changes in the Pacific Northwest. The coldest clumped isotope soil temperatures $T(\Delta_{47})$ (13.5 ± 1.9°C to 17.1 ± 1.7°C) occurred ~34,000–23,000 years ago. Using a soil-to-air temperature transfer function, we estimate Last Glacial Maximum (LGM) mean annual air temperatures of ~−5.5°C and warmest average monthly temperatures (i.e., mean summer air temperatures) of ~4.4°C. These data indicate a regional warming of 16.4 ± 2.6°C from the LGM to the modern temperatures of 10.9°C, which was about 2.5–3 times the global average. Proxy data provide locality constraints on the boundary of the cooler anticyclone induced by LGM ice sheets, and the warmer cyclone in the Eastern Pacific Ocean. Climate model analysis suggests regional amplification of temperature anomalies is due to the proximal location of the study area to the Laurentide Ice Sheet margin and the impact of the glacial anticyclone on the region, as well as local albedo. Isotope-enabled model experiments indicate variations in water $\delta^{18}O$ largely reflect atmospheric circulation changes and enhanced rainout upstream that brings more depleted vapor to the region during the LGM.

Plain Language Summary Warming and water isotope variations inferred from clumped isotopes are similar to transient climate model simulations for the Pacific Northwest from the Last Glacial Maximum to present. The amount of warming was larger than the global average and is likely due to the proximity of the site to the glacial margin.

1. Introduction

The Last Glacial Maximum (LGM; ~23,000-19,000 years ago; ka) is the subject of extensive study and represents a global climate state dramatically different from that of today, characterized by reduced greenhouse gas concentrations and extensive ice sheets (Mix et al., 2001; Raynaud et al., 1993). Proxy records and climate models show that glacial-interglacial cycles are driven by orbital forcing and internal mechanisms such as variations in insolation, greenhouse gas levels, and distribution of ice sheets (Cohmap Members, 1988; Lisiecki & Raymo, 2005; Mix et al., 2001; Weaver et al., 1998). To evaluate changing climatic conditions during the most recent glacial-interglacial cycle, several studies have examined sediments from different regions of North America from the LGM, ~23-19 ka (Clark et al., 2009; Clark & Mix, 2002; Mix et al., 2001) and the early Holocene (beginning 11 ka; Berger & Busacca, 1995; Blinnikov et al., 2002; Richardson et al., 1997; Spencer & Knapp, 2010; Sweeney et al., 2005). These studies identified that between the LGM and early Holocene there

Funding acquisition: Ricardo Lopez-Maldonado, Andre Ellis, Gregory Jesmok, Aradhna Tripati
Investigation: Ricardo Lopez-Maldonado, Hung-I Lee
Project Administration: Ricardo Lopez-Maldonado, Andre Ellis, Nicholas E. Bader, Pedro Ramirez, Gregory Jesmok, Aradhna Tripati
Supervision: Ricardo Lopez-Maldonado, Jesse Bloom Bateman, Andre Ellis, Nicholas E. Bader, Pedro Ramirez, Osinachi Ajoku, Gregory Jesmok, Clay Tabor, Aradhna Tripati
Visualization: Ricardo Lopez-Maldonado, Alexandrea Arnold, Osinachi Ajoku, Hung-I Lee, Deepshikha Upadhyay, Bryce Mitsunaga, Ben Elliott, Clay Tabor
Writing – original draft: Ricardo Lopez-Maldonado, Hung-I Lee
Writing – review & editing: Ricardo Lopez-Maldonado, Jesse Bloom Bateman, Andre Ellis, Nicholas E. Bader, Pedro Ramirez, Alexandrea Arnold, Osinachi Ajoku, Hung-I Lee, Gregory Jesmok, Deepshikha Upadhyay, Bryce Mitsunaga, Ben Elliott, Clay Tabor, Aradhna Tripati

were dramatic environmental changes including the collapse of the Cordilleran Ice Sheet (CIS) and Laurentide Ice Sheet (LIS), the drying out of major lake systems in the southwestern US and Great Basin regions, and increasing net precipitation (defined as the difference between precipitation and evaporation) in the Pacific Northwest (Lyle et al., 2012; McDonald et al., 2012; Whitlock, 1992).

However, despite decades of study, our ability to quantify and understand terrestrial climate variability in these and other midlatitude regions has been limited, largely because of ambiguous reconstructions, and disagreement between reconstructions and simulations. Two promising tools, carbonate clumped isotope thermometry and climate models, have the potential to help us quantify and understand regional terrestrial climate variability. Clumped isotope geochemistry investigates multiply substituted isotopologues, which are molecules that contain more than one heavy isotope (Eiler, 2011; Ghosh et al., 2006). Recent work has shown that carbonate clumped isotope thermometry, a paleotemperature proxy based on measurement of the degree of ordering of ^{13}C and ^{18}O with each other in carbonate minerals, can constrain the precipitation temperature of carbonate minerals without a priori knowledge of other environmental factors such as the oxygen isotope composition of carbonates and the waters from which they grew (e.g., Eiler, 2007; Ghosh et al., 2006). This technique can be applied to pedogenic carbonate horizons (Bk horizons) in soils from midlatitude settings, where carbonate formation is biased toward the warmer months (Breecker et al., 2009; Hough et al., 2014; Passey et al., 2010; Quade et al., 2013). Additionally, clumped isotope-derived precipitation temperatures can be combined with carbonate oxygen isotope data ($\delta^{18}O$; measured at the same time and on the same material as the clumped isotope measurement) with the known temperature-dependent fractionation of oxygen isotopes between carbonate and water (Epstein et al., 1953; Kim & O'Neil, 1997; McCrea, 1950) to determine the $\delta^{18}O$ of formation waters (Eiler, 2007).

Furthermore, clumped isotope-derived temperature estimates can be used in conjunction with climate model simulations like the Paleoclimate Modeling Intercomparison Project Phases 3 and 4 (PMIP3 and PMIP4) (Braconnot et al., 2012; Kageyama et al., 2018a) and the Transient Climate Evolution of the last 21,000 years (TraCE-21k) project (Liu et al., 2009), as well as comparing both temperature and water $\delta^{18}O$ with models that are isotope-enabled, and thus offer the ability to track processes impacting the water cycle via fractionations of oxygen and hydrogen isotopes (Brady et al., 2019; LeGrande & Schmidt, 2008; Roberts et al., 2011; Zhu et al., 2017). Clumped isotope-derived proxy data (including soil water temperature ($T(\Delta_{47})$), Mean Annual Air Temperature (MAAT), Warmest Average Monthly Temperature (WAMT; i.e., mean summer air temperatures), and the $\delta^{18}O$ of water in which the carbonate precipitated) can be compared to output from these three different models, in order to assess model-to-model accuracy in simulations of terrestrial hydroclimates (Eagle et al., 2013; Santi et al., 2020; Tripati et al., 2015).

Our study area is located in the Channeled Scablands-Palouse region (Figure 1). We chose this region because it was directly affected by the Purcell lobe of the CIS during the LGM, and thus provides critical constraints on potential climate responses to circulation changes induced by the collapse of the ice sheet (Alden, 1953; Lora et al., 2016; McDonald et al., 2012). This region preserves a sequence of late Pleistocene to Holocene pedogenic carbonates preserved in loess-paleosol sequences (sequences of fossil soils in deposits of aeolian silt). Figure 2 depicts the loess-paleosol sequences that were sampled, a legend describing their morphology, and the sampled depths. Since soils form from parent material by pedogenic processes that depend on local conditions (e.g., precipitation and heat flux) during the time of soil formation (Bader et al., 2015; Sheldon & Tabor, 2009), various proxy measurements of pedogenic carbonates have extensively been used as archives of paleoclimate data (Breecker et al., 2009; Cerling, 1984; Eagle et al., 2013; Passey et al., 2010; Peters et al., 2012; Quade et al., 2013; Sheldon & Tabor, 2009). Because paleosols containing pedogenic carbonate form over hundreds to thousands of years, their precipitation temperature depends primarily on the long-term mean climate; thus, short-term climatic variability does not overprint the long-term conditions (e.g., regional cooling due to volcanism; Peters et al., 2012; Sheldon & Tabor, 2009). By, creating additional paleoclimate records at this site, we are able to build on prior work examining controls on the stable isotopic composition of paleosols (Kelson et al., 2020; Passey et al., 2010) including on paleosols in this region (Lechler et al., 2018; Takeuchi et al., 2009). The chronology of the Palouse loess has also been well constrained by previous investigations (see Table S2 in Supporting Information S1) using a range of techniques, including paleomagnetism, radiocarbon, and thermoluminescence (Berger & Busacca, 1995; Blinnikov et al., 2002; Busacca, 1989; Richardson et al., 1997, 1999; Spencer & Knapp, 2010).

In this study, we use clumped isotope thermometry and $\delta^{18}O$ isotope measurements of glacial and deglacial pedogenic carbonates (i.e., hypocoatings; see A1. Microscale pedogenic carbonate in Supporting Information S1)

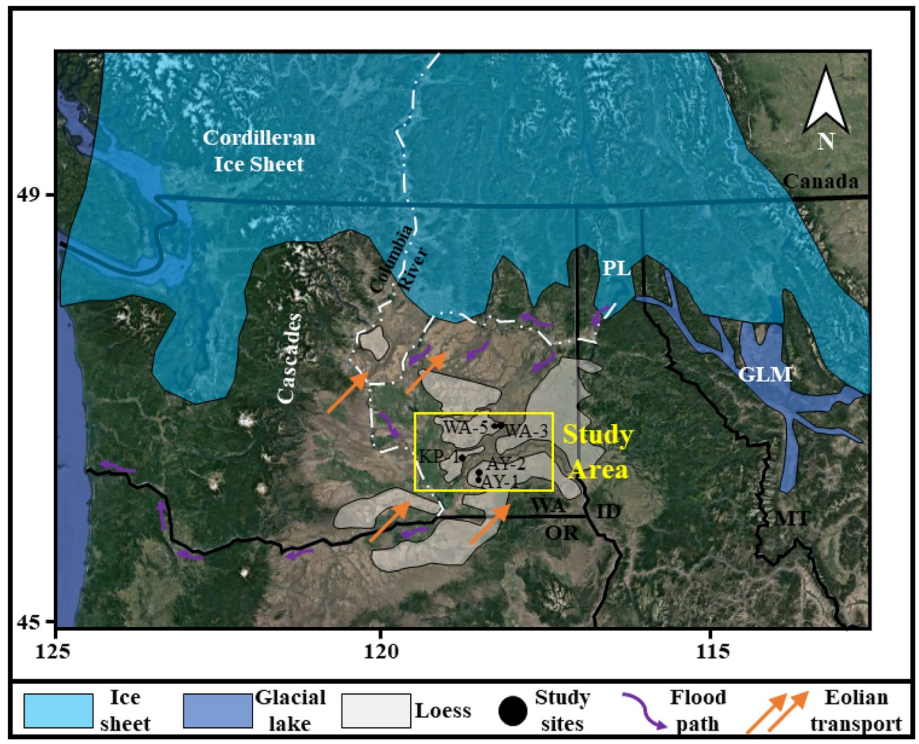

Figure 1. Locality map. Map of the Channeled Scablands-Palouse region showing the site locations within the context of Glacial Lake Missoula (GLM), the Cordilleran Ice Sheet (CIS) at its Late Wisconsin maximum, loess deposits, prevailing winds, and generalized flow directions.

from the Palouse loess with climate model simulations to examine the evolution of temperature and precipitation in the Pacific Northwest. We focused on the Washtucna paleosol that formed during the middle to late Wisconsin (~40 to 17 ka) and the Sand Hills Coulee that formed during both the Younger Dryas to early Holocene (~13 to 11 ka) and the relatively warm and dry Holocene Climatic Optimum (HCO; ~11 to 7 ka) (Berger & Busacca, 1995; Blinnikov et al., 2002; Richardson et al., 1997; Spencer & Knapp, 2010; Sweeney et al., 2005). Overall, our study included multiple objectives to better understand the temporal evolution in climate in the Palouse region. Our first objective was to utilize our proxy to: (a) reconstruct carbonate formation temperatures using carbonate clumped isotopes ($T(\Delta_{47})$); (b) to derive MAAT and WAMT using air temperature transfer functions developed by Quade et al. (2013); (c) to test paleotemperature results obtained from the Sand Hills Coulee paleosol to establish if it formed during the HCO as is generally assumed (Sweeney et al., 2005); Our second objective is to compare proxy data and climate model simulations, in which we: (a) compare derived MAAT and WAMT to modern and simulated regional mean annual temperature (MAT) and June, July, August temperature (JJA) and (b) compare reconstructed proxy data (i.e., $T(\Delta_{47})$, MAAT, WAMT, $\delta^{18}O$ of formation waters) to climate model simulations from the PMIP3 and PMIP4 project, the TraCE-21k project, and iCESM (Liu et al., 2009), to see what model output best matches proxy data for the region, given the spread of model results. Lastly, our study includes analysis of a climate model to allow for better understanding of the mechanisms responsible for the proxy signals by using both proxy-derived temperature and formation water $\delta^{18}O$ reconstructions and the stable water isotope-enabled version of the Community Earth System Model (iCESM1.2; Brady et al., 2019; Hurrell et al., 2013).

2. Background

The study area is within an 80 km^2 region at 46°N, 118°W with an average elevation of 420 m above average mean sea level in eastern Washington (Figure 1). The Palouse region currently experiences a temperate climate with a mean annual temperature of 10.9°C and a mean summer temperature of 21.2°C; mean annual precipitation is 280 mm with the majority occurring in winter (PRISM Climate Group, Oregon State University, 2021). Paleosol sites (Figure 2 and Table 1) include AY-1 (i.e., CLY-2 site in Busacca and McDonald (1994)), AY-2

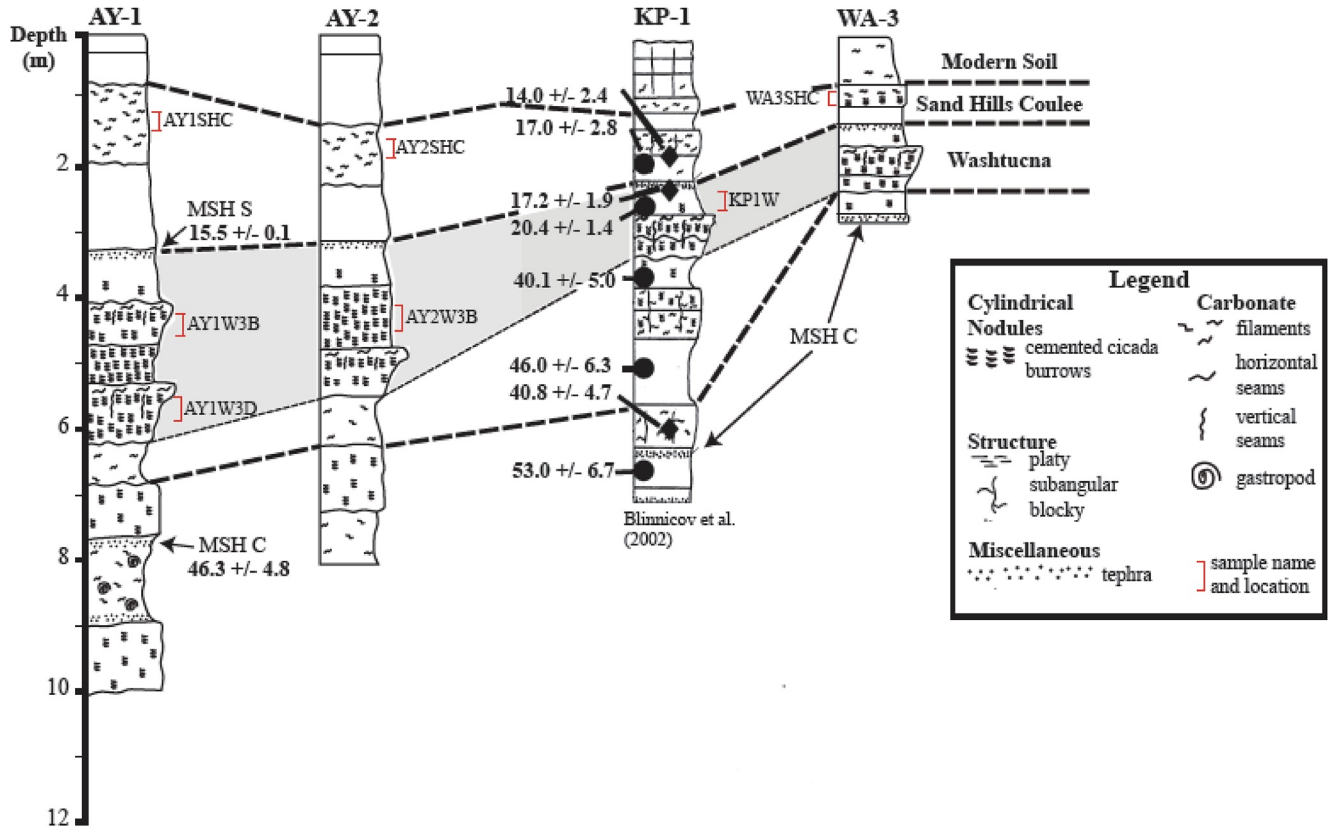

Figure 2. Pedostratigraphic columns with sampled locations, and sedimentation rate estimates. Thermoluminescence loess ages are in thousands of years (circles from Berger and Busacca (1995) and diamonds from Richardson et al. (1997, 1999)). The Mt. Saint Helens set S and C (MSH) tephra ages are in thousands of years. Sedimentation rate estimates from 35 ka to 15 ka (highlighted in gray) are estimated at approximately 6 cm per year, and before and after this interval, are estimated to be >20 cm per year (Table S3 in Supporting Information S1; Sweeney et al. (2004)). KP-1 was modified from Blinnikov et al. (2002), and WA-3 was modified from Busacca (1989).

(i.e., CLY-1 site in Busacca and McDonald (1994)), KP1, and WA-3 (i.e., Busacca's (1989) roadcut). Whitlock et al. (2000) and Blinnikov et al. (2002) compiled a terrestrial climate record of the region using a pollen record from Carp Lake and a phytolith (i.e., rigid, inorganic, microscopic silica remnants of plants) record from the Palouse loess, which provide context for this work. In addition, Dyke et al. (2002) describes the LIS and CIS margin advance and retreat. A composite ice sheet was created for the Coupled Model Intercomparison Project Phase 5 experiments by combining information from three reconstructions of the distribution of ice mass because direct evidence of the distribution does not exist (ICE-6G v2.0: Argus & Peltier, 2010; GLAC -1a: Tarasov et al., 2012; ANU: Lambeck et al., 2010).

Prior work has shown that the Palouse experienced cool, temperate, dry conditions during the early mid-Wisconsin (~42.9 to 30.9 ka), a point in time when the LIS margin was near the boundary of the Canadian Shield and the CIS remained small (Dyke et al., 2002). Toward the end of Oxygen Isotope Stage (OIS) 3 (36-27.6 ka) and the early stages of OIS 2 (beginning in 27.6 ka; Martinson et al., 1987), the LIS margin approximately followed

Table 1
Field Localities

Site	Paleosol material	Elevation (amsl ft)	Latitude	Longitude
AY-1	Micritic Carbonate/Carbonate Seam	1,255	46.312	−118.487
AY-2	Micritic Carbonate/Carbonate Seam	1,186	46.315	−118.490
WA-3	Micritic Carbonate/Carbonate Seam	1,583	46.767	−118.346
KP-1	Micritic Carbonate/Carbonate Seam	1,383	46.569	−118.627

Table 2
Estimated Sample Ages

Paleosol horizon and sample ID	Age (ka)	Uncertainty
Sand Hills Coulee Paleosol—Horizon Bkb1		
WA3SHC	12	1
KP1SHC	12	1.5
AY1SHC	9	2
AY2SHC	9	2
Washtucna Paleosol—Horizon Bwb2		
KP1W	17.2	1.9
Washtucna Paleosol—Horizon Bkqmb2 (upper)		
AY1W3B	23	3
WA3W	34	3
Washtucna Paleosol—Horizon Bkqb2		
AY2W3B	29	3
Washtucna Paleosol—Horizon Bkqmb2 (lower)		
AY1W3D	34	3

Note. Ages for samples were estimated using an age depth model constructed from using published geochronologic constraints in (Table S2 in Supporting Information S1) and sedimentation rates from Sweeney et al. (2004) (Table S3 in Supporting Information S1).

the boundary of the Canadian Shield and began its advance to its maximum extent (Dyke et al., 2002). The LIS margin advanced to its late OIS 2 limit in the northwest, south, and northeast (i.e., south of the of the Great Lakes) about 24-23 ka and in the southwest and far north about 21-20 ka (Dyke et al., 2002). It remained near that limit until ~17 ka, while the CIS remained limited (Clark & Mix, 2002; Dyke et al., 2002).

As the LIS retreated, the CIS advanced to its maximum extent at about 15-14 ka (Booth et al., 2003; Clark & Mix, 2002; Dyke et al., 2002; Whitlock, 1992). During this period (~30.9 to 15 ka), the Palouse experienced cold, dry conditions; in addition, the late Wisconsin Glacial Lake Missoula (15.7-13.5 ka) was created by an ice dam formed by the Purcell Trench lobe of the CIS (Blinnikov et al., 2002; Booth et al., 2003; Whitlock et al., 2000). Near the end of OIS 2 and the beginning of OIS 1 (14 ka; Martinson et al., 1987), the climate in the Palouse transitioned into a cooler and wetter climate that persisted throughout the late glacial period (~14 to 11 ka; i.e., the Younger Dryas to early Holocene). Thereafter, the climate progressed into a warmer and drier climate than the modern (see Table S4 in Supporting Information S1) that persisted throughout the HCO (~11 to 7 ka).

The Palouse loess was likely sourced from slack-water sediments (i.e., sands and silts that settled from suspension at locations of reduced local flow velocities) deposited during glacial outburst floods in basinal areas (i.e., Pasco Basin and Walla Walla Valley to the south and southwest, especially near Wallula Gap) (Bader et al., 2016; McDonald & Busacca, 1992; Spencer & Knapp, 2010; Sweeney et al., 2007). These floods were created from the rapid emptying of Glacial Lake Missoula by recurring hydraulic instability (Booth et al., 2003). After the deposition of slack-water sediments, prevailing southwesterly wind transported these deposits from the basinal areas onto the surrounding Palouse hills (McDonald et al., 2012; Sweeney et al., 2007). Times of decreased eolian dust production may have allowed episodes of soil formation in the loess, which appear to have occurred primarily during full glacial conditions when the North American ice sheets produced a glacial anticyclone resulting in weakened westerly winds (Bartlein et al., 1998; Sweeney et al., 2004). Slowing loess transport and deposition process promoted calcic soil formation despite the cold climate (Sweeney et al., 2004). Dust production decreased up to fivefold (~6 cm/yr) from 35-15 ka and increased afterward to a rate greater than 20 cm/yr (Sweeney et al., 2004; Table S3 in Supporting Information S1).

The entire Palouse loess spans the Pleistocene and Holocene (Berger & Busacca, 1995; Blinnikov et al., 2002; Busacca, 1989; Richardson et al., 1997, 1999; Spencer & Knapp, 2010). Table 2 summarizes the estimated sample ages and Table S2 in Supporting Information S1 summarizes chronologic constraints. Different sections of the Palouse loess have been dated using a range of techniques, including paleomagnetism, radiocarbon, and thermoluminescence. Two markers (i.e., Cascade-sourced tephras [i.e., volcanic erupted silicate rock fragments] and distinct carbonate paleosols like the Washtucna and the Old Maid Coulee paleosols) were used in the field to correlate horizons that have not been dated at sites being investigated in this study (McDonald et al., 2012; Spencer & Knapp, 2010). In addition, estimated sedimentation rates (see Table S3 in Supporting Information S1) from Sweeney et al. (2004) were applied between datums to estimate the age of horizons lacking an absolute age date. In summary (Figure 2), the main dated tephra layers for the sites being investigated include the Mt. Saint Helens set C (MSH C; cal. 46.3 ± 4.8 ka), and Mt. Saint Helens set S (MSH S; cal. 15.4 ± 0.1 ka; McDonald et al., 2012; Sweeney et al., 2005). Surrounding sites, not investigated in this study, either contain the Glacier Peak tephra (cal. 11.6 ± 0.05 ka), or the Mazama Ash (cal. 7.6 ± 0.1 ka; McDonald et al., 2012; Sweeney et al., 2005). Additional age control was provided from thermoluminescence dating of quartz and feldspar grains (Berger & Busacca, 1995; Richardson et al., 1997, 1999). Thermoluminescence age on the lower boundary of the Washtucna paleosol is 40.1 ± 3.7 ka, and an age for the upper boundary is 17.2 ± 1.9 ka (Richardson et al., 1997, 1999). A thermoluminescence age on the lower boundary of the Sand Hills Coulee paleosol is 14.0 ± 2.4 ka (Richardson et al., 1997); however, the upper boundary is not well constrained, and appears to possibly extend into the HCO.

3. Materials and Methods

3.1. Field Methods

The sites were prepared for sampling by excavating all visibly weathered or modern material from the surface of the soil profile in order to expose comparatively unaltered loess (Bader et al., 2015). The sites are not described in this study, but we do provide pedostratigraphic columns in Figure 2, because detailed descriptions already exist from previously published literature (Busacca, 1989; Busacca & McDonald, 1994; McDonald & Busacca, 1992). Carbonate development in the field was assessed based on visible calcic features and sample effervescence in 5% HCl. Micrite and microsparite field samples were segregated from horizontal and vertical carbonate seams in Bk horizons and used for clumped isotope analysis (Supporting Information S1). In addition, two supplemental analyses, Mg/Ca and Mn/Ca ratios (Li et al., 2013), and micromorphology analysis of thin sections stained with alizarin red-s and potassium ferricyanide, were used to discriminate pedogenic carbonate from detrital carbonate (Figures S1–S6 and Table S1 in Supporting Information S1).

3.2. Calculation of Isotopic Ratios and Temperatures

Detailed methodology can be found in the Supporting Information S1. In brief, powdered paleosol samples were measured during the course of 28 days in four correction intervals on a modified MAT 253 IRMS mass spectrometer and 8 days in one correction interval on a Nu Perspective gas-source IRMS mass spectrometer. In each case, samples were digested in a common acid bath at 90°C, with temperature drift monitored using a thermocouple and checked daily prior to analysis. Resultant CO_2 was purified to remove: water vapor using a series of cryogenic traps, sulfur compounds using silver wool, and other trace contaminants using a Thermo Trace GC Ultra gas chromatograph column filled with Porapak-Q. Purified gas was then passed on to the mass spectrometer for analysis, with the MAT 253 measuring nine acquisitions per measurement replicate, with 10 cycles per acquisition (working gas-sample measurements) and the Nu Perspective measuring four acquisitions per measurement replicate, with 20 cycles per acquisition. Equilibrated gas and a suite of carbonate standards were measured every 2–4 analyses during each run, using methods described elsewhere (Defliese & Tripati, 2020; Upadhyay et al., 2021). For this work, samples were replicated with a minimum of three measurements each, unless the amount of sample limited analyses, following the approach of Huntington et al. (2009).

Raw data were corrected using Easotope (John & Bowen, 2016). Data are reported using the Brand parameter set (Daeron et al., 2016) and reported on the Intercarb-Carbon Dioxide Equilibrium Scale (ICDES) (Bernasconi et al., 2021). We use internal standards calibrated against NBS-19 for drift correction for $\delta^{13}C$ and $\delta^{18}O$. These corrections are typically 0.04‰ for $\delta^{13}C$ and 0.3‰ for $\delta^{18}O$ (see Upadhyay et al., 2021 for more details). Nonlinearity in the mass spectrometers was corrected using equilibrated gas standards (25 and 1,000°C) and a pair of carbonate standards (ETH 1 and 2; 600°C). An empirical transfer function was created using the ETH 1–4 standards (Bernasconi et al., 2021) and a suite of in-house carbonate standards (Lucarelli et al., 2021) to project the data into the ICDES reference frame. Overall, the accuracy of our lab standards, or long-term mean absolute error, is 0.0002‰, and the long-term external reproducibility for the Δ_{47} of lab standards is better than 0.02‰ (S.D.) and 0.006‰ (S.E.) (Upadhyay et al., 2021). Stable and clumped isotope measurements for all standards used to correct values within this study can be found in Table S7 in Supporting Information S1. Final Δ_{47} values were converted into paleotemperatures using temperature calibration of Anderson et al. (2021) and the carbonate-water oxygen-isotope calibration relationship of Kim and O'Neil (1997) was used for reconstructing formation water $\delta^{18}O$. Data are reported with one standard error, which reflects the external reproducibility of all replicates for $T(\Delta_{47})$ and formation water $\delta^{18}O$.

Calculated soil carbonate formation temperatures (referred to as $T(\Delta_{47})$) were then used to reconstruct MAAT and WAMT by using the relationship published by Quade et al. (2013; see Table S4 in Supporting Information S1). Note that we use WAMT, instead of mean summer air temperatures, to remain consistent with the terminology chosen by Quade et al. (2013). The relationships between $T(\Delta_{47})$, and MAAT and WAMT were established by Quade et al. (2013) by correcting $T(\Delta_{47})$ results for soil depth from a single profile because daily and seasonal air temperatures attenuate significantly with soil depth. The corrections taken by Quade et al. (2013) resulted in an effective air temperature that was highly correlated to local air temperatures based on the analysis of modern soils sampled from Arizona, Nevada, Tibet, Pakistan, and India. Because $T(\Delta_{47})$ can be used to construct effective air temperatures, which in turn are highly correlative with local air temperatures

of modern soils, past climate MAAT and WAMT can therefore be reconstructed from $T(\Delta_{47})$ by using the relationships established by Quade et al. (2013). Note that Quade et al. (2013) selected soils from a wide range of climate and soil water regimes to ensure that their results have a broad applicability to interpreting $T(\Delta 47)$ from ancient soils for which seasonality is not known. Uncertainties for the transfer functions from soil $T(\Delta_{47})$ to MAAT and WAMT are not reported in the original publication, thus, uncertainties in $T(\Delta_{47})$, MAAT, and WAMT errors are reported as one standard error and represent propagated external errors from clumped isotope analysis, following conventions from several studies (Eagle et al., 2013; Passey et al., 2010). The interpretation of MAAT, and WAMT, is dependent on the robustness of the transfer functions, though quantifying potential systematic biases is a challenge.

3.3. Model Simulations

We compared data to simulations from nine PMIP3 models and, at the time of writing, four currently available PMIP4 models (Braconnot et al., 2012) to assess the regional climate in these simulations. PMIP3 and PMIP4 LGM model simulations differ from each other in the specification of the ice sheets reconstructions used within each experiment (Kageyama et al., 2021). PMIP3 models used a composite of three reconstructions to model ice sheets during the LGM (Abe-Ouchi et al., 2015), while all PMIP4 models used in this study utilized a new model (ICE-6G_C; Peltier et al., 2015) which reduced the altitude of the ice sheets relative to the original PMIP3 studies (Kageyama et al., 2021). We compared reconstructed glacial to modern temperature changes to the changes in simulated temperatures between LGM and preindustrial simulations (LGM-PI). In addition, we compared MAAT and WAMT derived from our samples to Pacific Northwest temperatures from the transient climate simulation of the last 22 ka (TraCE-21k; He, 2011; Liu et al., 2009), which uses the NCAR Community Climate System Model Version 3 (CCSM3). To examine water isotopes and gauge the impact of ice sheets on temperatures in the region of interest, we also performed simulations with the Community Earth System Model version 1.2 (iCESM1.2) with water isotope tracers (Brady et al., 2019). Isotopes of oxygen and hydrogen are included in the dynamically coupled atmosphere (CAM5), ocean (POP2), land (CLM4), sea ice (CICE4), and river runoff (RTM) components. For this work, the atmosphere and land are on a 1.9° latitude × 2.5° longitude finite-volume grid, and the ocean and sea ice use a ∼1° rotated pole grid. Previous studies show that the simulated isotopic distributions compare favorably with observation and other models of similar complexity (Brady et al., 2019; Nusbaumer et al., 2017; Wong et al., 2017). We performed three simulations: (a) a preindustrial control (PI) experiment, (b) a LGM experiment with period appropriate boundary conditions, and (c) a LGM land-ice only (LGM-ice_only) experiment, using the LGM ice sheet configuration with PI CO_2 and orbital conditions. Coastlines and sea levels are implemented by the oceanic and atmospheric/land surface models but are amended by comparing with the geological records in LGM (Kageyama et al., 2018b). Initial ocean oxygen isotopic distributions came from the GISS interpolated ocean $\delta^{18}O$ data set (LeGrande & Schmidt, 2006). Ocean average $\delta^{18}O$ was increased by +1‰ for the LGM and LGM-ice_only experiments to account for the large ice sheets (Duplessy et al., 2002). Ice volume and topography came from the ICE-6G data set (Peltier et al., 2015). All simulations were initialized from previous experiments and run for an additional 550 years with water isotope tracers, allowing the atmosphere, land, and upper ocean to reach near equilibrium; data analyzed are from the final 48 years of each simulation.

To quantitatively gauge climate model performance, we calculated the skill score for temperature anomalies estimated by each of the models considered in this study using the equation:

$$\text{Skill score (SS)} = 1 - \sqrt{\frac{\Sigma(m_i - o_i)^2 - \Sigma\left(e_i^2\right)}{\Sigma(n_i - o_i)^2 - \Sigma\left(e_i^2\right)}}$$

where m_i are the model results, n_i are the reference (in our case, $n_i = 0$, with no change from the LGM to modern), o_i are the observations (clumped results), and e_i are the observation uncertainties (Hargreaves et al., 2013; Lora et al., 2017). A skill score of 1 represents a perfect model, where there is no disagreement between clumped and model estimates, a negative skill score demonstrates that the errors in the model are greater than the reconstructions and a skill score that is undefined would indicate that the model and clumped estimates are too close to evaluate within error of the observations.

Table 3
Stable Isotope Data Summary

Sample name	# Replicates	# Acquisitions	$\delta^{13}C_c$ (‰) (V-PDB)	1 S.D.	$\delta^{18}O_o$ (‰) (V-PDB)	1 S.D.	Δ_{47} (‰; ICDES)[a]	1 S.E.
AY1SHC	4	36	−4.3	0.1	−12.4	0.1	0.546	0.008
AY1W3B	6	54	−6.3	0.0	−13.5	0.1	0.630	0.006
AY1W3D	12	108	−5.7	0.1	−12.1	0.2	0.619	0.006
AY2SHC	11	84	−4.3	0.2	−11.3	0.2	0.560	0.006
AY2W3B	2	18	−5.4	0.1	−12.4	0.20	0.616	0.007
AY2W3C[b]	5	45	−4.4	0.2	−11.8	0.1	0.568	0.006
KP1SHC[b]	6	44	−2.5	0.1	−12.4	0.1	0.514	0.009
KP1W	8	57	−4.3	0.2	−13.0	0.4	0.606	0.005
WA3SHC	3	22	−6.5	0.1	−13.7	0.3	0.620	0.009
WA3W[b]	7	63	−4.5	0.1	−12.8	0.1	0.575	0.004

Note. All units for isotope ratios in per mil. Errors are propagated. Acquisitions represent a block of multiple sample-working gas cycle comparisons, and vary based on the instrument used (nine for Thermo 253, four for Nu Perspective IRMS).
[a]ICDES = Intercarb-Carbon dioxide equilibrated scale. [b]Likely impacted by detrital/dissolution based on petrography/ancillary geochemistry (Lopez-Maldonado, 2017).

4. Results

4.1. Carbonate $\delta^{18}O$ and Temperature Changes: Proxy Data

Measured stable isotope ratios of carbonates are in Table 3 and are presented on the VPDB scale. The $\delta^{18}O$ of carbonates range from −13.3‰ to −11.3‰. The $\delta^{18}O$ of carbonates are higher (−12.4‰ to −12.1‰) during the latter part of OIS-3 (36-27.6 ka) as well as during OIS-2 (27.6-14 ka) (−13.5‰ to −13.0‰) relative to modern values from Takeuchi et al. (2009) (−14.2‰ to −13.3‰). OIS-1 (14 ka-present) carbonates have similar or higher $\delta^{18}O$ values (−13.7‰ to −11.3‰). Carbonate $\delta^{18}O$ values are consistent with two previous studies in the region (Stevenson, 1997; Takeuchi et al., 2009).

Calculated formation water isotope values are in Table 4 and are presented on the VSMOW scale. The $\delta^{18}O$ of formation waters ranges from −13.5 to −6.6‰ (VSMOW). During the latter part of OIS-3 (36-27.6 ka), the $\delta^{18}O$ of formation waters stabilized at −11.4‰ ± 1.3‰, while during OIS-2 (27.6-14 ka) at an estimated age of 23 ± 3 ka the $\delta^{18}O$ of formation waters was reduced (−13.5‰ VSMOW). At an estimated age of 17.2 ± 1.9 ka (during OIS-2) the $\delta^{18}O$ of formation waters (−11.5 ± 1.1‰ VSMOW) was similar to the $\delta^{18}O$ of formation

Table 4
Stable Isotope-Derived Reconstructions of Hydroclimate Parameters

Sample name	Age (ka)	Err	Δ_{47}-T (°C)[a]	1 S.E.	$\delta^{18}O_w$ V-SMOW[b]	1 S.D.	MAAT (°C)[c]	WMAT (°C)[c]
AY1SHC	9	2	42.8	3.3	−6.6	1.2	—	—
AY2SHC	9	2	37.4	2.3	−6.6	1.5	—	—
Average	*9*	*2*	*40.1*	*3.8*	*−6.6*	*0.0*	—	—
WA3SHC	12	1	16.6	2.7	−13.1	0.6	−1.8	7.9
KP1W	17.2	1.9	20.9	1.5	−11.5	1.1	3.4	12.8
AY1W3B	23	3	13.5	1.9	−13.5	1.0	−5.5	4.4
AY2W3B	29	3	17.9	2.1	−11.4	0.6	−0.2	9.5
AY1W3D	34	3	17.1	1.7	−11.4	1.2	−1.1	8.6

Note. Errors are propagated.
[a]Calculated using an equation from Anderson et al. (2021). [b]Calculated using an equation of Kim and O'Neil (1997). [c]Calculated using an equation from Quade et al. (2013). Three samples from Table 3 that are impacted by detrital carbonate or dissolution are not included.

waters (−13.1 ± 0.6‰ VSMOW) at the estimated age of 12 ± 1 ka during the early part of OIS-1 (14 ka-present). Toward the middle of OIS-1, at an estimated age of 9 ± 2 ka the $\delta^{18}O$ of formation waters were higher, relative to samples in earlier intervals (−6.6‰ VSMOW).

Clumped isotope-derived soil $T(\Delta_{47})$, MAAT and WAMT estimates utilizing a soil-to-air temperature transfer function from Quade et al. (2013) are in Table 4. Three samples were likely impacted by detrital carbonate or dissolution based on petrography/ancillary geochemistry, thus, we do not utilize these samples to estimate paleotemperatures and have excluded them from Table 4. Clumped isotope soil $T(\Delta_{47})$ range from 13.5 ± 1.9°C to 42.8 ± 3.3°C. Paleoclimate reconstruction of air temperatures derived from soil temperatures using the relationship published from Quade et al. (2013) include a MAAT range from −5.5°C to 29.7°C, and a WAMT range from 4.4°C to 37.6°C. Our data from the oldest sampled Washtucna paleosol horizon, with an estimated age of 34 ± 3 ka, suggest that carbonate formed at a soil $T(\Delta_{47})$ of 17.1 ± 1.7°C with a calculated MAAT of −1.1°C and a WAMT of 8.6°C. At the estimated age of 29 ± 3 ka, the Washtucna paleosol data suggest that carbonate formed at an equivalent soil $T(\Delta_{47})$ of 17.9 ± 2.1°C, with a calculated MAAT of −0.2°C, and a WAMT of 9.5°C. $T(\Delta_{47})$ yielded lower carbonate temperatures of formation in the Washtucna paleosol with an estimated age of 23 ± 3 ka, suggesting that carbonate formed at a soil $T(\Delta_{47})$ of 13.5 ± 1.9°C, with a calculated MAAT of −5.5°C, and a WAMT of 4.4°C. The youngest sampled paleosol horizon, with an estimated age 17.2 ± 1.9 ka, yielded a soil $T(\Delta_{47})$ of 20.9 ± 1.5°C, with a calculated MAAT of 3.4°C, and a WAMT of 12.8°C. The Sand Hills Coulee paleosol horizon, with an estimated age of 12 ± 1 ka, suggest that carbonate formed at a soil $T(\Delta_{47})$ of 16.6 ± 2.7°C, with a calculated MAAT of −1.8°C. Two similarly aged Sand Hills Coulee paleosol horizons with an estimated age of 9 ± 2 ka yielded different temperatures from soil $T(\Delta_{47})$, which averaged out to 40.1 ± 3.8°C. Paleoclimate MAAT and WAMT were not derived for the youngest Sand Hills Coulee sample, as discussed in Section 5.1.

4.2. Temperature Changes: Climate Models

Temperatures from climate models come from the nearest grid cell to our study location and are reported in Tables S5 and S6 in Supporting Information S1. The TraCE-21k model simulations yielded an LGM to preindustrial change of 7.4°C for MAAT, and 6.8°C for the WAMT, while absolute temperatures change from −6.6°C to 0.8°C for MAAT and 3.6–10.4°C for WAMT. Temperatures increased across OIS-2 (27.6-14 ka) from minimum values of −6.7°C to −1.7°C for MAAT and 3.6–11.4°C for WAMT. Absolute values during OIS-1 (14 ka to present) ranged from −1.7°C to 1.0°C for MAAT and 10.4–12.2°C for WAMT.

The simulations for iCESM yielded an LGM to preindustrial change of 13.2°C for MAAT, and 8.8°C for the WAMT, while absolute temperatures results shift from −6.2°C to 7.0°C for MAAT and 9.6–18.4°C for WAMT.

The PMIP3 models yield a LGM to preindustrial change in MAAT that ranged from 5.1°C (for model CNRM-CM5) to 17.6°C (for model MIROC-ESM), and the ensemble mean anomaly value is 12.9°C. Absolute LGM temperatures ranged between −12.8°C (for the model COSMOS-ASO) and 3.2°C (for the model CNRM-CM5). The ensemble mean yielded a PMIP3 LGM MAAT of −5.9°C. The PMIP4 models yield a LGM to preindustrial change in MAAT of 5.1°C (for model MPI-ESM-1-2-LR) to 9°C (for models MIROC-ES2L and INM-CM4-8), and the ensemble mean value is 8°C. Absolute LGM temperatures ranged between −1.1°C (for the model MIROC-ES2L) and 1.7°C (for the model AWI-ESM-1-1-LR). The ensemble mean yielded a PMIP4 LGM MAAT of −0.3°C.

5. Discussion

5.1. Comparison to Regional Proxy Records

Clumped isotope data over the past 36,000 years reveal evidence for dynamic changes in temperature in the region (Figures 3a and 3b). The quantitative reconstruction of temperature from the clumped isotope data reveals a pattern of change that is consistent with other clumped isotope (Lechler et al., 2018) and qualitative, nonthermodynamically derived proxy records (i.e., pollen and phytolith data) (Blinnikov et al., 2002; Whitlock et al., 2000). The temperature change we find is similar to, but slightly smaller (by ∼2°C) than what was inferred by Lechler et al. (2018) average temperatures (i.e., LGM and Holocene) using clumped isotopes $T(\Delta_{47})$. Note that we excluded the $T(\Delta_{47})$ results from the youngest samples we collected from the SHC (9 ± 2 ka) (as discussed

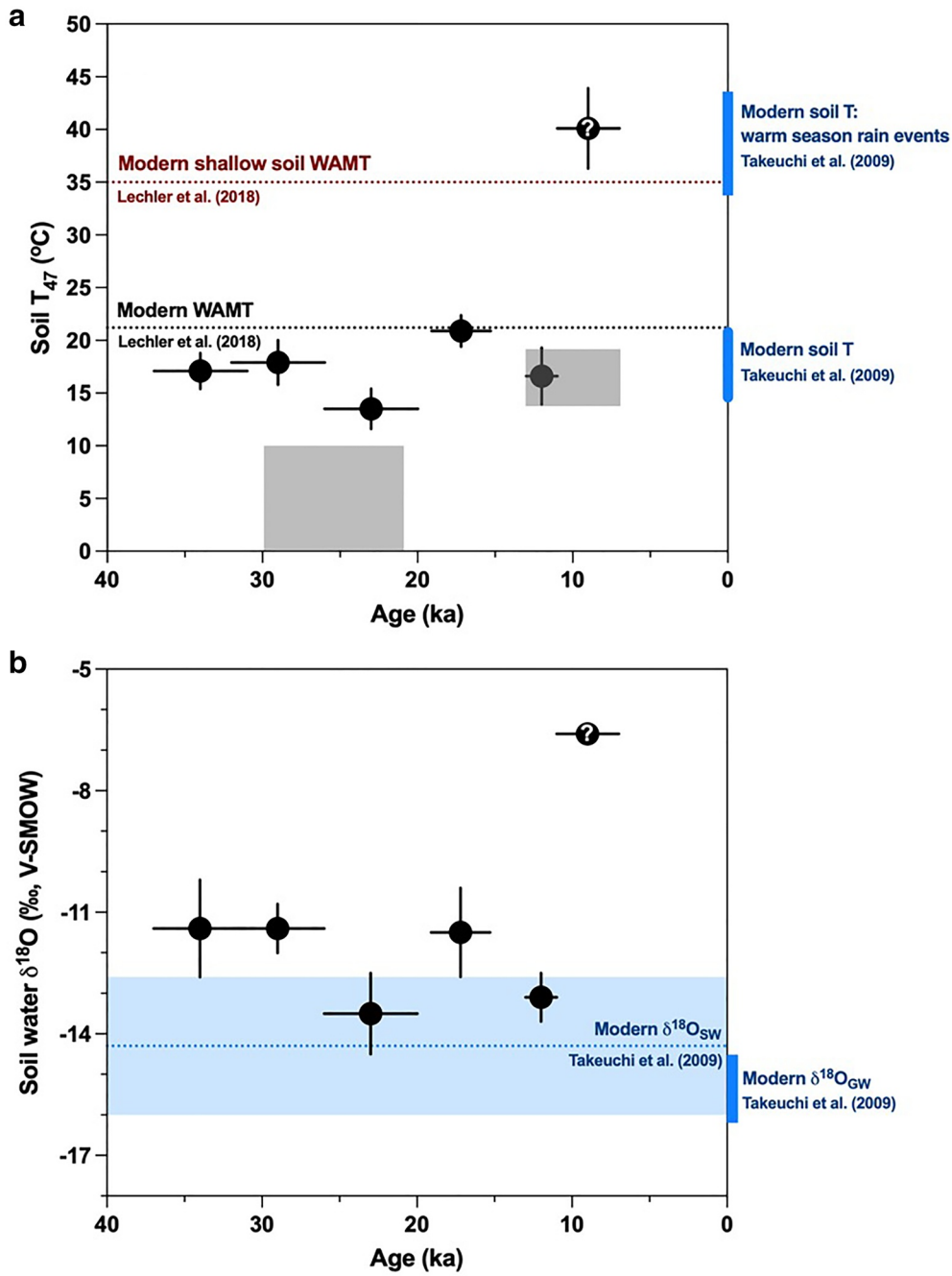

Figure 3. Estimates of soil carbonate formation temperatures from clumped isotopes (Soil $T(\Delta_{47})$) and water $\delta^{18}O$ over the past 40 ka. (a) Black circles indicate soil carbonate formation temperatures results from this work calculated using our measurements of $T(\Delta_{47})$ and the temperature calibration from Anderson et al. (2021). Black symbol with question mark indicates data from samples that formed during the Holocene Climatic Optimum, that could record formation during conditions similar to modern season rain events in shallow soils, after Lechler et al. (2018), or could be impacted by radiative heating effects. Shaded gray boxes indicate temperatures reconstructed by Lechler et al. (2018). Blue vertical bars on the right indicate modern soil temperatures associated with carbonate precipitation derived from modern Palouse loess soil water samples and soil carbonates from Takeuchi et al. (2009). Black dotted line indicates modern warm month mean temperatures, while blue dotted line indicates temperatures during modern warm season rain events, and red dotted line indicates modern shallow soil warm month mean temperatures, after Lechler et al. (2018). (b) Black circles indicate results calculated using the carbonate-water $\delta^{18}O$ calibration of Kim and O'Neil (1997). Blue dotted line with blue shading indicates modern soil water $\delta^{18}O$ and groundwater $\delta^{18}O$ from Takeuchi et al. (2009), respectively. Blue vertical bar on the right indicates modern groundwater $\delta^{18}O$ from Takeuchi et al. (2009).

at the end of this section), and included samples collected by Lechler et al. (2018) from CLY-1/3 at depths of 4.08 m, and 5.88 m with $T(\Delta_{47})$ of 24 ± 3°C and 28 ± 3°C, respectively, in the LGM average.

Our data also provide further resolution on both the magnitude and timing of variations inferred by pollen and phytolith data sets. The data, as shown in Figures 3a and 3b provide quantitative evidence to support the qualitative hydroclimate reconstructions from pollen in nearby Carp Lake, where a transition in vegetation type occurred from the LGM to modern that would reflect a change to a hotter, drier environment (Whitlock et al., 2000). The temperature shift in Figures 3a and 3b matches the timing of changes in paleoclimate inferred from phytoliths in the Palouse loess (Blinnikov et al., 2002), where colder conditions prevailed throughout the LGM and deglaciation, but a switch to warming occurred during the Holocene. The clumped isotope reconstruction is also broadly consistent with inferences of temperature change from other proxies including chironomids and pollen (Meltzer & Holliday, 2010). Figure 3a also depicts Takeuchi et al. (2009) modern carbonate precipitation temperatures which were derived using the equilibrium oxygen isotope calcite-water fractionation factors from Friedman and O'Neil (1977) and historical local temperature records. Figure 3b depicts Takeuchi et al. (2009) measured modern $\delta^{18}O$ of formation waters. Our clumped isotope-derived soil temperature estimates during the LGM and deglaciation are broadly similar to the modern average soil temperature estimates presented in Takeuchi et al. (2009), while our Holocene-aged sample aligns with estimates of soil temperature during warm season rain events (Figure 3a).

The soil temperatures recorded during the pre-LGM indicate $T(\Delta_{47})$ of 17.1 ± 1.7°C with a calculated MAAT of −1.1°C and a WAMT of 8.6°C. Note that this sample (AY1W3D) is a composite of samples collected by Lechler et al. (2018) from CLY-1/3 at depths of 5.55 and 5.88 m with $T(\Delta_{47})$ of 8 ± 2°C and 28 ± 3°C, respectively. Whitlock et al. (2000) describes a cool-temperate, dry climate from phytolith data that lasted from 42.9 to 30.9 ka. Quantitative proxy temperatures from $T(\Delta_{47})$ record an amplified cooling at an estimated age of 23 ± 3 ka with values of 13.5 ± 1.9°C and a calculated MAAT of −5.5°C and a WAMT of 4.4°C. Note that Lechler et al. (2018) averaged a LGM $T(\Delta_{47})$ of 9 ± 4°C that was collected from the same pedostratigraphic horizon as this sample (AY1W3B), excluding the samples collected at 4.08 and 5.55 m depth. The pollen record from Carp Lake also records a change that reflects a cold, much drier environment that lasted from 30.9 to 13.2 ka. Soil temperatures warm slightly to pre-LGM levels by 17.2 ± 1.9 ka, at a time that Blinnikov et al. (2002) describes as the late glacial interval. The Sand Hills Coulee paleosol horizon with an age of 12 ± 1 ka yields a $T(\Delta_{47})$ of 16.6 ± 2.7°C and a derived MAAT of −1.8°C and a WAMT of 7.9°C. Note that Lechler et al. (2018) collected two samples from CLY-1/3 section of a similar age with $T(\Delta_{47})$ of 19 ± 3°C and 16 ± 3°C. Regional proxy data suggests the late glacial interval (~14 to 11 ka; i.e., the Younger Dryas to early Holocene), while warmer than the LGM, had cooler and wetter conditions relative to modern. Ultimately, the cooler and wetter conditions gave way to drier than modern conditions in the early Holocene (11–7 ka; Blinnikov et al., 2002). The Sand Hills Coulee paleosol horizons with an estimated age of 9 ± 2 ka, from the HCO, yield an average $T(\Delta_{47})$ of 40.1 ± 3.8°C. Note that our Sand Hills Coulee paleotemperatures appear unusually warm, in contrast to samples collected by Lechler et al. (2018) that yield an average $T(\Delta_{47})$ of 18 ± 2°C. Blinnikov et al. (2002) finds that Pinus-Quercus woodland developed around Carp Lake after 9 ka, during the HCO, and observed an increase in sagebrush from the mid-Holocene (6ka) near the sites investigated in this study, implying drier and warmer conditions than today. The qualitative results are consistent with the Sand Hills Coulee paleosol horizon data (Figures 3a and 3b, white symbol). The magnitude of warmth for our Sand Hills Coulee $T(\Delta47)$ values we attribute to reflect, at least in part, radiative heating and shallow soil processes.

5.2. Regional Amplification of Cooling and Warming

A global synthesis of terrestrial and marine proxy data combined with the ensemble of PMIP2 climate models suggest global MAAT temperatures during the LGM were ~4°C cooler than modern (Annan & Hargreaves, 2013; Bartlein et al., 2011; Braconnot et al., 2007; Shakun et al., 2012) (Figure 4), while more recent proxy syntheses and model analysis suggests it may have been cooler than the PMIP2 model projections, with estimates ~5°C to 6.5°C cooler than modern (Friedrich et al., 2016; Tierney et al., 2020). Furthermore, the first proxy-constrained, dynamically consistent and spatiotemporally climate change model estimates an even larger degree of cooling, with LGM air temperatures estimated at ~7°C cooler than modern (Osman et al., 2021). The clumped isotope data for the Palouse during the latter part of OIS-3 and the beginning of OIS-2 (27.6-21 ka) would imply a much larger amplitude of regional temperature change (16.4°C cooler MAAT during the LGM relative to modern

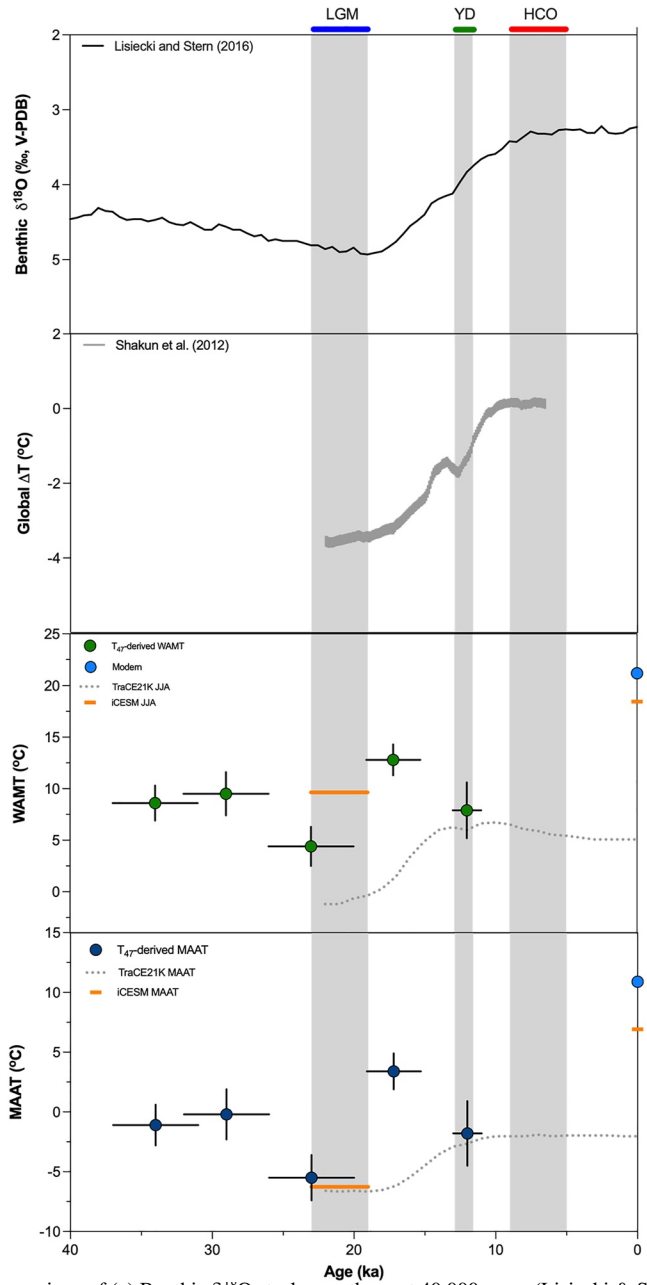

Figure 4. Multiproxy comparison of (a) Benthic $\delta^{18}O$ stack over the past 40,000 years (Lisiecki & Stern, 2016). (b) Global temperatures derived from a synthesis of different paleoclimate proxies from Shakun et al. (2012), with larger amplitude (~5°C to 6.5°C) changes estimated by Friedrich et al. (2016) and Tierney et al. (2020); Absolute temperature estimates from this study (uncertainties are in 1 S.E.) of (c) warmest average monthly temperatures (WAMT) and (d) mean annual air temperatures (MAAT) derived from clumped isotopes $T(\Delta_{47})$ compared to absolute regional TraCE21k and iCESM temperatures from simulations. Last Glacial Maximum (LGM), Younger Dryas (YD), and Holocene Climatic Optimum (HCO) are marked above the plot, and the respective time intervals within the plot are denoted as vertical Gy bars TraCE21k temperatures are shown with dotted line (Liu et al., 2009). iCESM temperatures are shown with orange horizontal bars. Green, dark blue, and white circles indicate WAMT and MAAT values. Light blue circles indicate modern values for MAAT (10.9°C) and WAMT (21.2°C) (Prism Climate Group). Mean LGM WAMT (JJA) = 1°C $T(\Delta_{47})$, −6.2°C (iCESM), −6.6°C (TraCE21k). Mean present day (or preindustrial simulation) JJA = 18.4°C (iCESM), 10.4°C (TraCE21k). Mean LGM MAAT = −9.2°C $T(\Delta_{47})$, −6.2°C (iCESM), −6.6°C (TraCE21k). MAAT YD = −0.9°C $T(\Delta_{47})$, HCO = 17.1°C $T(\Delta_{47})$. WAMT YD = 8.8°C $T(\Delta_{47})$, HCO = 25.8°C $T(\Delta_{47})$. LGM-PD MAT is −12.9°C (PMIP3 Ensemble), −8.0°C (PMIP4 Ensemble), −13.2°C (iCESM), −7.4°C (TraCE). LGM-PD WAMT is 8.8°C (iCESM), 6.8°C (TraCE).

values obtained from the 30-year normal (1991–2020) Prism Climate Group (10.9°C)) than either of these estimates for global surface temperatures. The larger MAAT regional amplitude change is a relevant finding in this study because the data are broadly consistent with a range of qualitative proxies such as pollen records (Whitlock et al., 2000) and phytoliths (Blinnikov et al., 2002), as well as published clumped isotope data from Lechler et al. (2018).

Large-scale Northern Hemisphere changes associated with global climatic events have been linked to dramatic changes in regional water budgets and aridity (Asmerom et al., 2010; Lora et al., 2016; Lyle et al., 2012; Munro & Laabs, 2013; Reheis et al., 2014; Santi et al., 2020; Wagner et al., 2010; Whitlock & Bartlein, 1997). The larger amplitude of cooling in the Channeled Scablands-Palouse region during the latter part of OIS-3 and the beginning of OIS-2 (~27.6 to 21 ka) coincides with a culmination of different events that would have strongly impacted regional climates. During the latter part of OIS-3 and the beginning of OIS-2, the last LIS buildup took place when the ice margin was at a proximal location to the study area (Bartlein et al., 1998; Dyke et al., 2002; Hostetler & Bartlein, 1999). During this time, anticyclonic circulation would have been produced by high sea level pressure over the ice sheet, and the westerly jet over the eastern portion of western North America would have been split (Bartlein et al., 1998; Hostetler & Bartlein, 1999; Manabe & Broccoli, 1985) and shifted equatorward (Gray et al., 2020; Lora et al., 2016). Weakened westerlies due to the anticyclone decreased loess deposition rates at sites >150 km from the LIS margin, therefore, demonstrating weakened westerly winds extended as far south as the Washington and Oregon border from ~36 to 15 ka (Sweeney et al., 2004). Moreover, dry conditions, inferred from pollen and phytoliths records, would have resulted from the anticyclone deflecting moisture-bearing storms from the Washington and Oregon to the southwest (Lora et al., 2016, 2017; Sweeney et al., 2004; Tabor et al., 2021; Whitlock & Bartlein, 1997).

The coldest temperatures (e.g., MAAT −5.5°C and WAMT 4.4°C) in Channeled Scablands-Palouse region reached their peak during the LGM (~23 + 3 ka), with warming in the region occurring thereafter coeval with a decrease in a global benthic $\delta^{18}O$ stack (Lisiecki & Stern, 2016) and synthesis of proxy data (Shakun et al., 2012) (Figure 4). Using a suite of 10Be surface exposure ages from boulder surfaces in terminal moraines Ullman et al. (2015) pinpointed the initial retreat of the southern margin of the ice sheet in the Wisconsin to 23.0 + 0.6 ka (Stokes, 2017). The initial retreat of the ice margin was synchronous with several other locations along the southern margin and coincided with the initial increase in summer insolation around 24-23 ka (Ullman et al., 2015). As the southern margin was beginning to retreat, Murton et al. (2007), Kennedy et al. (2010), and Lacelle et al. (2013) found that there is strong evidence that the margin in the far northwest was still advancing and likely attained its maximum position after 18.5 ka. Ullman et al. (2015) also pointed out that an acceleration in retreat after around 20.5 ka was likely driven by acceleration in boreal summer insolation and that this occurred before any increase in atmospheric CO_2, supporting an orbital forcing trigger for initial deglaciation argued by Clark et al. (2009) and Gregoire et al. (2015). The temperatures in Channeled Scablands–Palouse region at ~17.2 + 1.9 ka warmed to a MAAT of 3.4°C and a WAMT of 12.8°C. Ullman et al. (2015) identifies an acceleration in the ice sheet retreat after around 20.5 ka, but it's important to clarify that the ice margin retreat remained relatively slow prior to ~17 ka (Stokes, 2017).

The ice sheet margin retreated rapidly between around 16 and 13 ka, particularly along the southern and western margins, which led to the separation of the Laurentide from the Cordilleran Ice Sheet (Stokes, 2017). Our data suggest that temperatures during the Younger Dryas were warmer than LGM values, but cooler than post-LGM and at present. The temperatures in Channeled Scablands-Palouse region at ~12 + 1 ka warmed to a MAAT of −1.8°C and a WAMT of 7.9°C. Lora et al. (2016) argues that the shift toward a warmer global climate (Diffenbaugh et al., 2006; Kaufman et al., 2004; Marcott et al., 2013; Mayewski et al., 2004; Shakun et al., 2012), and regionally to a warmer, wetter climate, began to occur after a rapid deglaciation around 14 ka; identified by Blinnikov et al. (2002) as the late glacial interval. Lora et al. (2016) show that an abrupt transition of the simulated circulation occurs in direct response to a sudden drop in North American continental ice. These changes in turn would have led to an abrupt reorganization of the atmospheric circulation, during which time the two branches of the westerly jet merged and shifted poleward by several degrees, moistening the Pacific Northwest (Lora et al., 2016). This is consistent with the relationship of the jet stream and storm track with equator-to-pole temperature gradients, through the thermal wind relationship and baroclinic instability, respectively. A poleward retreat of land ice would have weakened meridional temperature gradients, leading to a migration of the jet stream further north. Recent work using climate models to dissect mechanisms for LGM hydroclimate changes in Western North America has shown that ocean-atmosphere feedbacks would have played a pivotal role in resulting

hydroclimate changes, including through impacts on North Pacific sea surface temperatures that in turn affect rainfall patterns (Amaya et al., 2021). In addition, a reduction of land-ice would influence coastal sea surface temperatures through changes in sensible-heat fluxes (Yanase & Abe-Ouchi, 2010).

Data show this warmer, wetter climate around 14 ka (Lora et al., 2016), identified by Blinnikov et al. (2002), ultimately gave way to drier than modern conditions; the warmest temperatures (e.g., MAAT 26.4°C and WAMT 34.5°C) in Channeled Scablands-Palouse region reached their peak during the HCO at ~9 + 2 ka when Blinnikov et al. (2002) observes an increase in sagebrush phytoliths around the sites investigated in this study, implying a drier climate than modern and an increase in exposure to solar heating of the soil surface (Hough et al., 2014; Figures 4c and 4d). The HCO temperatures that we reconstruct are similar to or warmer than present (Figures 4c and 4d). A major factor associated with regional terrestrial hydroclimate changes during the early and mid-Holocene is insolation driven by Earth's orbital variations (Diffenbaugh et al., 2006; Kaufman et al., 2004; Mayewski et al., 2004; Skinner et al., 2020), and changes in atmospheric circulation have been inferred from proxy and model analysis (Bartlein et al., 1998; Kaufman et al., 2004; Skinner et al., 2020). A weakening of the Aleutian low in winter, identified by Lora et al. (2016) as beginning by 13.5 ka, and the strengthening of the eastern Pacific and Bermuda high-pressure systems in summer, along with evidence for a poleward shift in atmospheric rivers in the mid-Holocene (Skinner et al., 2020) associated with the northward movement of the jets, would have created conditions that were less cloudy and drier than present in the region, which ultimately caused hotter near-surface air temperatures (Bartlein et al., 1998). Furthermore, heat capacity during this period of higher summer insolation increased as a result of more vegetated land and changes in soil moisture associated with ice sheet retreat (Gildor & Tziperman, 2001; Kaufman et al., 2004). Atmospheric warming is thought to have triggered the initial retreat of the LIS; however, Ullman, Carlson, Anslow, et al. (2015) surface energy balance model found that the net surface mass balance was positive until after 11.5 ka, which implies that mass loss was primarily driven by dynamic discharge via calving at marine-terminating ice streams. Ullman, Carlson, Anslow, et al. (2015) argues that only when summer temperatures increased by 6–7°C (relative to the LGM) did the LIS ice sheet's surface mass balance become increasingly negative in the early Holocene, which occurred between 11.5 and 9 ka, and very rapid retreat of the ice sheet occurred after ~9 ka was driven by surface melt rather than dynamic discharge.

5.3. Proxy Temperatures Compared to Simulations

Between the LGM and PI there is greater warming in the Pacific Northwest than in the global average in all model simulations (see Figures S7 and S8 in Supporting Information S1). Six out of nine models from the PMIP3 ensemble and iCESM simulated colder MAAT changes in excess of 10°C, and two of the PMIP4 models showed changes greater than ~9°C at our study region (48.5°, −118.5°W) (Figure 5 and Table S6 in Supporting Information S1). The LGM to PI MAAT anomaly at the sample site is 12.9 ± 4.6°C (1 S.D.) and 8.0 ± 2.0°C (1 S.D.), for the PMIP3 and PMIP4 multimodel ensemble mean, respectively. Reconstructed PMIP4 temperature anomalies are smaller in comparison to PMIP3 models in extratropical North America, which has been hypothesized to be due to change in North American Ice sheet reconstructions within PMIP4 models (Kageyama et al., 2021). The PMIP3 model ensemble MAAT anomaly at our site is comparable to, but slightly smaller in magnitude (−12.9 ± 4.6°C), than the LGM to present day temperature anomaly seen in derived MAAT reconstructed from clumped isotope data from this study (−16.4 ± 1.9°C) with the difference not being statistically significant given the uncertainties. Five of the PMIP3 models that simulated the largest changes (i.e., CCSM4, FGOALS-g2, IPSL-CM5A-LR, MIROC-ESM, and MPI-ESM-P) compare favorably to our result (Table S6 in Supporting Information S1). The PMIP3 simulation results for changes in WAMT are similar, except that the inter-model spread is greater. The LGM-PI WAMT anomaly in the multimodel ensemble average of PMIP4 is −7.2 ± 2.4°C (1 S.D.), which is much smaller than the ensemble average WAMT anomaly in the PMIP3 multimodel average of −12.9 ± 9.0°C (1 S.D.), and our estimate of WAMT temperature anomaly of −16.8 ± 1.9°C.

Figure 5 (top panel) shows the evaluation of the LGM-PI MAAT anomaly for each model relative to our clumped isotope temperature anomalies (colored bars), and relative to clumped isotope anomalies from this study and pollen data from Bartlein et al. (2011; white bars). Overall, most models demonstrate a positive skill score with respect to the clumped isotope reconstructed temperatures, showing that both the model and clumped isotope-derived temperature anomalies are larger than the observational uncertainties and of the same sign. The PMIP3 multimodel average (SS = 0.82) had an overall higher skill score than the PMIP4 multimodel average (SS = 0.50), when compared to clumped isotope data. The PMIP3 multimodel average (SS = 0.38) and PMIP4

10.1029/2021PA004266

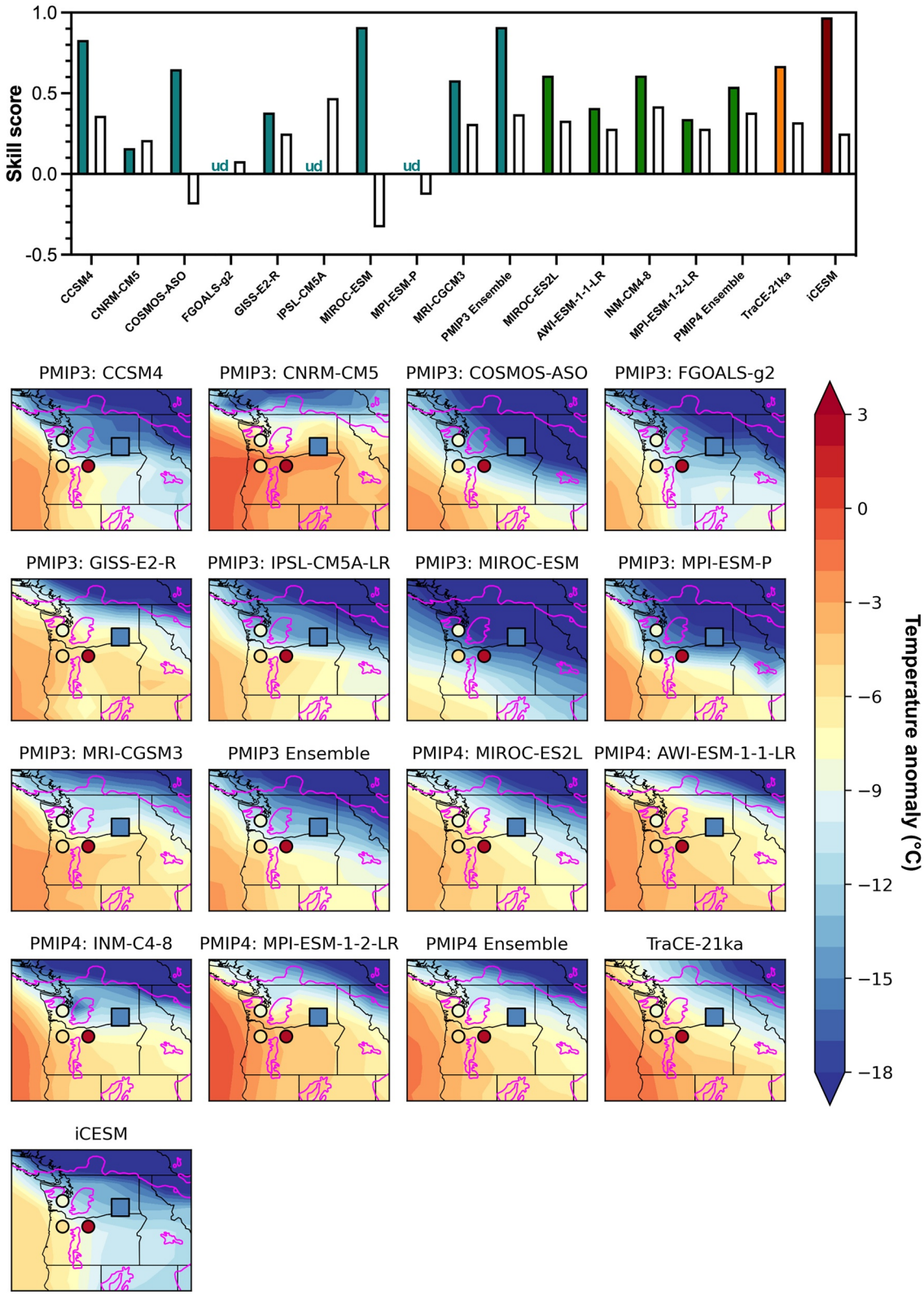

Figure 5. Proxy-model comparison. Top: Model skill score calculated for temperature anomaly after Hargreaves et al. (2013) and Lora et al. (2017). Coloring of bars shows grouping of climate models simulations for different experiments. Samples that are undefined with respect to skill are indicated with ud and show the model and clumped-derived estimates are too close to evaluate within error of the observations. Colored bars indicate comparison to clumped isotope data, while white bars indicate comparison to both clumped isotope data from this study and pollen data from Bartlein et al. (2011). Bottom: Temperature anomaly for available models (PMIP3, PMIP4, TraCE-21k, iCESM) compared to clumped isotope (square; this study) and pollen data (circles; Bartlein et al., 2011). Ice boundaries in magenta.

multimodel average (SS = 0.37) were similarly skilled when evaluated using a combination of clumped isotope and pollen data but had lower skill scores than when compared with only the clumped isotope reconstructed temperatures. Only three PMIP3 models (MIROC-ESM, MPI-ESM-P, and COSMOS-ASO) exhibit negative skill when evaluated using clumped isotope and pollen data.

We also compared our proxy data to the transient evolution of mean and warmest month temperatures from TraCE-21k and iCESM (Figures 4c and 4d). Our MAAT and WAMT results follow the same broad pattern of temperature change as the TraCE simulation, with a warming trend through the last deglaciation. However, the proxy temperature estimates for MAAT show significantly larger-magnitude changes than the TraCE simulation results. On the other hand, WAMT proxy temperatures and the TraCE simulation show similar temperatures during the LGM and approximately 12 ka, and smaller-magnitude changes than the TraCE simulation at approximately 17 ka. The iCESM reconstructs slightly higher LGM MAAT temperatures, but significantly higher LGM WAMT temperatures.

Disagreement in the absolute values of temperature that may result from the low resolution of models, or potentially point to unresolved model and/or proxy biases. At midlatitude and high-latitude settings, carbonate formation occurs during the warmer months (Breecker et al., 2009; Hough et al., 2014; Kelson et al., 2020; Passey et al., 2010; Quade et al., 2013), including in this region as has been established by prior in-depth studies (Lechler et al., 2018; Takeuchi et al., 2009). However, it is possible that the transfer functions that are used to convert from seasonally biased $T(\Delta_{47})$ to MAAT, which are based on modern data from sites from a broad array of latitudes (Quade et al., 2013), may be inaccurate for sites that are relatively proximal to ice sheet margins, or for the LGM. Climate models also can struggle to capture proxy-reconstructed warmth, possibly due to an inability to accurately simulate vegetation changes (Tabor et al., 2021). Ultimately, proxy system models (Fischer-Femal & Bowen, 2021) coupled to simulations may help to resolve the origin of this disagreement. Nevertheless, the broad-scale agreement between the transient simulation and our reconstruction supports the overall general accuracy of the regional climate changes simulated by TraCE-21k (Figures 4c and 4d).

To better understand the mechanisms responsible for the proxy signals, we compared our measurements against outputs from LGM, LGM-ice_only, and PI iCESM model simulations (see Section 2 and Figure 6). For temperatures in the region, LGM-ice_only produces about 66% as much cooling relative to PI as the full LGM simulation (Figures 6a and 6b), implying that a significant portion of the LGM temperature signal is a consequence of topographic and albedo changes. We also suggest that the ice sheets alone explain part of the local precipitation reduction at the LGM as the regional pattern of precipitation response is quite similar between the LGM and LGM-ice_only cases (Figures 6c and 6d), a consequence of similar atmospheric circulation changes (discussed above in Section 5.2). Likewise, $\delta^{18}O$ from precipitation ($\delta^{18}O_p$) responses demonstrate that a large portion of the LGM depletion signal relates to the presence of the ice sheets (Figures 6e and 6f). The local $\delta^{18}O$ of column integrated vapor has a large depletion value relative to PI for both the LGM and LGM-ice_only cases ($-3.66‰$ and $-2.98‰$, respectively), suggesting the ice sheets play an important role bringing depleted moisture to the region. Greater rainout of moisture as it moves inland from the Pacific, related to enhanced land-sea horizontal temperature gradients and circulation changes, appears to drive much of the depletion seen in column integrated vapor and $\delta^{18}O_p$ at the LGM (Tabor et al., 2021). Although the specific causes of isotopic changes in the region are complex, it is clear that the North American ice sheets are an important driver of the regional signal. Like the temperature response, the proximity of the site to the ice edge leads to an amplified deglacial response in $\delta^{18}O_p$.

5.4. Implications for the Boundary of the LGM Anticyclone

Determining the regions that were influenced by the glacial anticyclone, given disagreements between model simulations, remains a major essential challenge. Cyclonic wind anomalies in the Eastern Pacific, driven by the decreasing sea level pressure (Lora et al., 2017), bring warm air toward the west coast of the US. The warm air is mostly blocked by Pacific coastal mountain ranges, and turns into the northwest US. The easterly wind anomalies, driven by LGM ice, would have delivered cold air toward the west US, as observed in the PMIP3 model ensemble 850 mbar anomalies (LGM-preindustrial) shown in Figure 7. However, the Rocky Mountains, stretching from Idaho to Colorado, insulate most of the cold air.

Our study area, as it resides in a basin between the Pacific coastal ranges and the Rockies, provides constraints on the boundary of the glacial anticyclone induced by LGM ice sheets, between the cooler LGM anticyclone anomaly relative to the warmer cyclone anomaly in the Eastern Pacific Ocean. We compare the MAAT

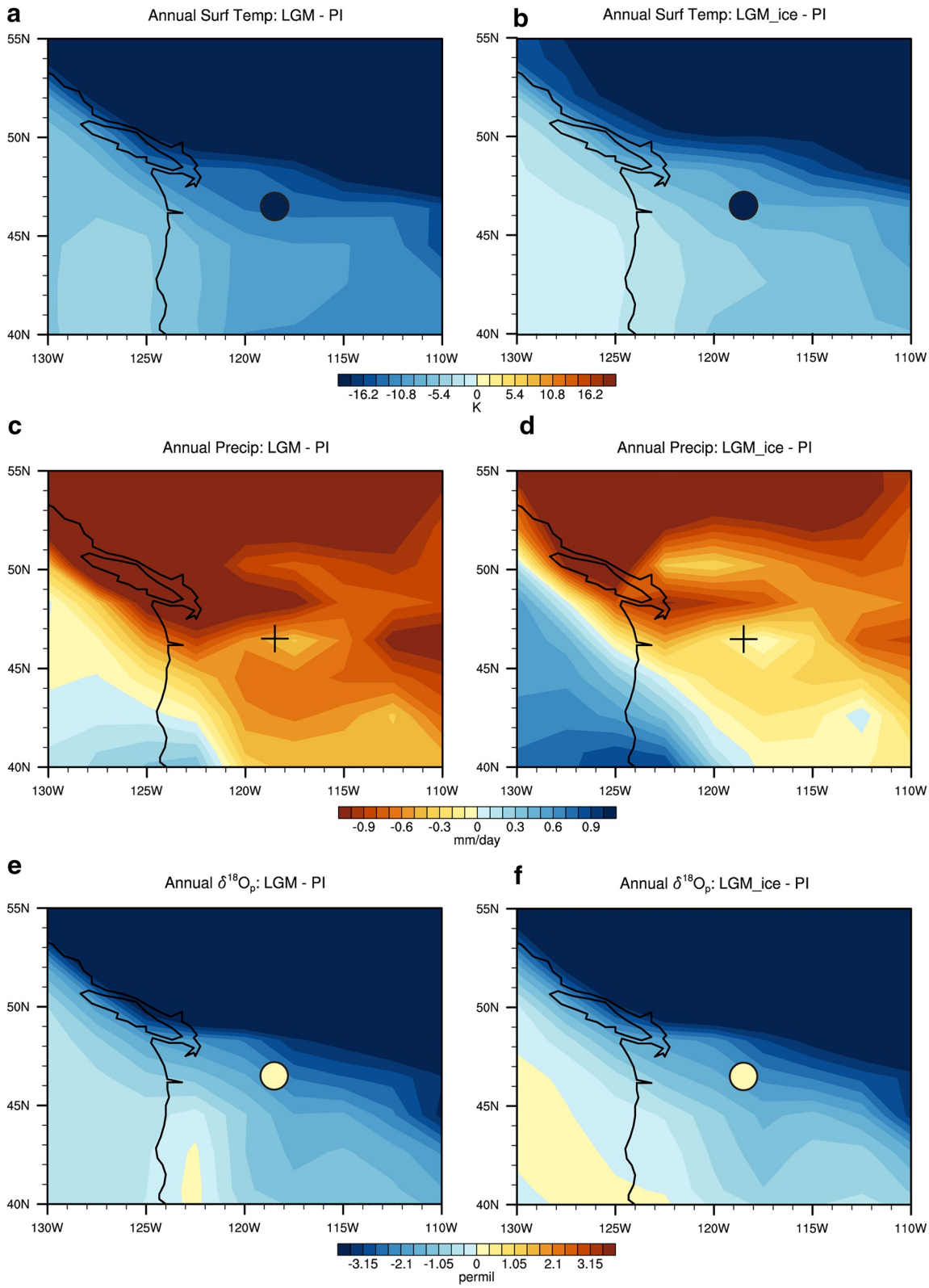

Figure 6. LGM iCESM 1.2 simulations compared to clumped isotope-derived estimates at sample site (circles). Crosses are shown to denote the study site where there is no comparative estimate from clumped isotope analysis. (a) Annual average surface temperature anomalies (LGM minus preindustrial). (b) Annual average surface temperature anomalies (LGM_ice minus preindustrial). (c) Precipitation anomalies (LGM minus preindustrial). (d) Precipitation anomalies (LGM_ice minus preindustrial). (e) $\delta^{18}O_p$ anomalies (LGM minus preindustrial). (f) $\delta^{18}O_p$ anomalies (LGM_ice minus preindustrial) the Holocene (Liu et al., 2009).

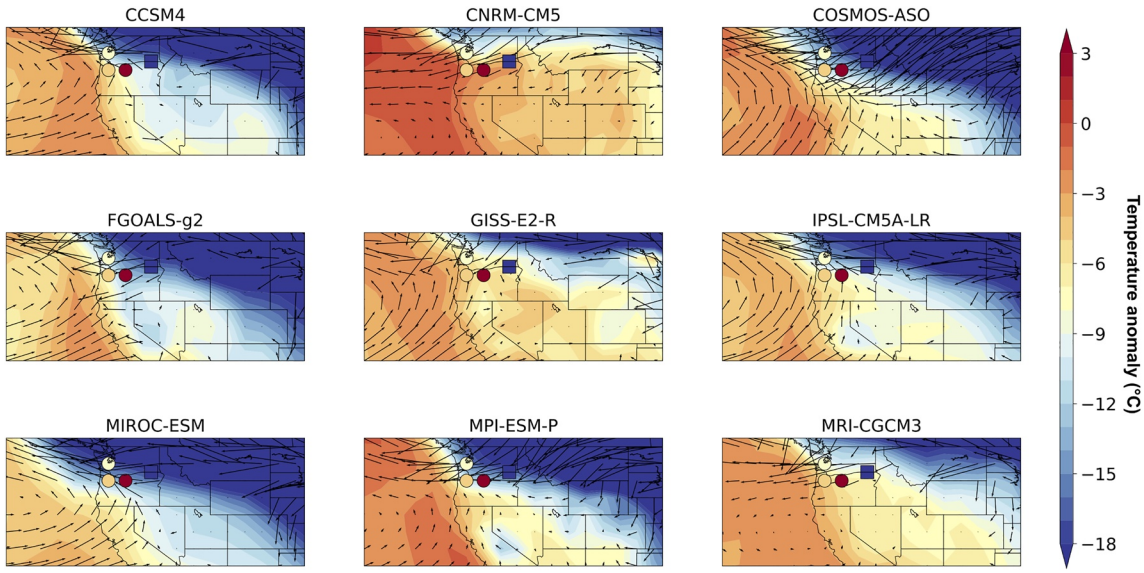

Figure 7. Near surface (850 mb) wind anomaly (black arrows) for PMIP3 models, in concert with data shown in Figure 5: LGM minus preindustrial MAAT anomalies for PMIP3 (colorful contours), pollen reconstruction (circle), and clumped isotope (square) with near surface (850 mb) wind anomaly for PMIP3 (black arrows).

reconstruction derived from clumped isotopes to pollen data (Bartlein et al., 2011) for three sites to the west (Figure 7). The weaker MAAT anomalies at pollen record sites indicate that these regions are mostly dominated by west to east flows of warmer air from the Eastern Pacific. However, the MAAT anomaly drops dramatically at our study site, consistent with evidence from the thick accumulation of loess in the region, suggesting coverage by the glacial anticyclone during the LGM. Given the dramatic difference between MAAT anomalies between the three pollen localities and our study area, it is likely that the boundary of the LGM ice-dominated and Eastern Pacific-dominated regimes passed through central Oregon and Washington. Obtaining clumped isotope temperature reconstructions at the three pollen localities from Bartlein et al. (2011) in future studies will provide evidence for any disagreements between the temperature reconstructions. These data imply climate models such as FGOALS-g2 may overestimate the strength of glacial anticyclone driven by LGM ice, as they simulate cold air that flows into the entire Central Valley and Death Valley regions of California, while other models such as GISS-E2-R may simulate the warm air from the Eastern Pacific penetrating too far inland.

6. Conclusions

This study provides novel paleoenvironmental constraints for the Pacific Northwest, a region that was proximal to the ice sheet margin during the LGM, from clumped isotope analysis and water isotope-enabled simulations. We use clumped isotope measurements of paleosols to reconstruct temperatures and water isotope values from soil carbonates ~36 to 9 ka in age. At the LGM, when mean annual surface temperature changed globally by 4–7°C, $T(\Delta_{47})$ suggests that regional MAAT and WAMT changed by around 2.5 to 3 times this amount in our study area. Calculated soil carbonate formation temperatures, MAAT, and WAMT exhibit a pattern of change from ~36 ka to modern that correlates with paleoenvironmental constraints from pollen and phytoliths as well as with model simulations. Model-data comparison indicates the magnitude of temperature change is likely explained by the proximity of the study area to the LIS margin, the resulting influence of the glacial anticyclone on the region, and local albedo, while changes in the isotopic composition of precipitation largely reflect depleted column integrated vapor during the LGM, likely due to atmospheric circulation changes and enhanced rainout as moisture moves inland.

Data Availability Statement

The iCESM model data presented in this manuscript are available in the Zenodo repository (Tabor, 2021). Reconstructed climate parameters and proxy data from Tables and Supporting Tables will be archived at the NOAA's NCEI World Data Service for Paleoclimatology on acceptance at Lopez-Maldonado et al. (2022), https://doi.org/10.25921/r09x-m706.

Acknowledgments
We thank Alex Lechler and Kate Huntington for discussions of this work. RLM was partially supported by the NSF CREST Center for Energy and Sustainability at Cal State LA (HRD-0932421). This work was supported by NSF CAREER award EAR-1352212, NSF ICER-1936715, Heising-Simons Foundation 2021–3137 and 2022–3314 to AT, and the "Laboratoire d'Excellence" LabexMER (ANR-10-LABX-19) and the French government ("Investissements d'Avenir"). We thank members of the Tripati lab group for their support. Development of the stable water isotope-enabled version of the Community Earth System Model was made possible by the National Science Foundation (NSF) Grants AGS-1401778, AGS-1401803, and AGS-1401802. Clay Tabor acknowledges funding from the National Center for Atmosphere Research Advanced Study Program postdoctoral fellowship and NSF Grant AGS-1804747. The CESM project is supported primarily by the National Science Foundation (NSF). This material is based upon work supported by the National Center for Atmospheric Research, which is a major facility sponsored by the NSF under Cooperative Agreement No. 1852977. Computing and data storage resources, including the Yellowstone and Cheyenne supercomputers (https://doi.org/10.5065/D6RX99HX), were provided by the Computational and Information Systems Laboratory (CISL) at NCAR.

References

Abe-Ouchi, A., Saito, F., Kageyama, M., Braconnot, P., Harrison, S. P., Lambeck, K., et al. (2015). Ice-sheet configuration in the CMIP5/PMIP3 last glacial maximum experiments. *Geoscientific Model Development*, *8*(11), 3621–3637. https://doi.org/10.5194/gmd-8-3621-2015

Alden, W. C. (1953). Physiography and glacial geology of Western Montana and adjacent areas (U.S. Geol. Surv. Prof. Pap. 231, pp. 142–153). https://doi.org/10.3133/pp231

Amaya, D. J., Alexander, M. A., Capotondi, A., Deser, C., Karnauskas, K. B., Miller, A. J., & Mantua, N. J. (2021). Are long-term changes in mixed layer depth influencing North Pacific marine heatwaves? *American Meteorological Society*, *102*(1), 59–66. https://doi.org/10.1175/bams-d-20-0144.1

Anderson, N. T., Kelson, J. R., Kele, S., Daëron, M., Bonifacie, M., Horita, J., et al. (2021). A unified clumped isotope thermometer calibration (0.5–1,100°C) using carbonate-based standardization. *Geophysical Research Letters*, *48*, e2020GL092069. https://doi.org/10.1029/2020GL092069

Annan, J. D., & Hargreaves, J. C. (2013). A new global reconstruction of temperature changes at the Last Glacial Maximum. *Climate of the Past*, *9*(1), 367–376. https://doi.org/10.5194/cp-9-367-2013

Argus, D. F., & Peltier, W. R. (2010). Constraining models of postglacial rebound using space geodesy: A detailed assessment of model ICE-5G (VM2) and its relatives. *Geophysical Journal International*, *181*, 697–723. https://doi.org/10.1111/j.1365-246x.2010.04562.x

Asmerom, Y., Polyak, V. J., & Burns, S. J. (2010). Variable winter moisture in the southwestern United States linked to rapid glacial climate shifts. *Nature Geoscience*, *3*(2), 114–117. https://doi.org/10.1038/ngeo754

Bader, N., Nicolaysen, K. P., Lopez-Maldonado, R., Murray, K. E., & Mudd, A. C. (2015). Extensive middle Miocene weathering interpreted from a well-preserved paleosol, Cricket, Oregon, USA. *Geoderma*, *239–240*, 195–205. https://doi.org/10.1016/j.geoderma.2014.10.007

Bader, N., Spencer, P. K., Bailey, A. S., Gastineau, K. M., Tinkler, E. R., Pluhar, C. J., & Bjornstad, B. N. (2016). A loess record of pre-Late Wisconsin outburst flooding, Pleistocene paleoenvironment, and Irvingtonian fauna from the Rulo site, southeasten Washington, USA. *Palaeogeography, Palaeoclimatology, Palaeoecology*, *462*, 57–69. https://doi.org/10.1016/j.palaeo.2016.08.042

Bartlein, P. J., Anderson, K., Anderson, P., Edwards, M., Mock, C., Thompson, R., et al. (1998). Paleoclimate simulations for North America over the past 21,000 years: Features of the simulated climate and comparisons with paleoenvironmental data. *Quaternary Science Reviews*, *17*(6–7), 549–585. https://doi.org/10.1016/s0277-3791(98)00012-2

Bartlein, P. J., Harrison, S. P., Brewer, S., Connor, S., Davis, B. A. S., Gajewski, K., et al. (2011). Pollen-based continental climate reconstructions at 6 and 21 ka: A global synthesis. *Climate Dynamics*, *37*(3), 775–802. https://doi.org/10.1007/s00382-010-0904-1

Berger, G. W., & Busacca, A. J. (1995). Thermoluminescence dating of late Pleistocene loess and tephra from eastern Washington and southern Oregon and implications for eruptive history of Mount St. Helens. *Journal of Geophysical Research*, *100*(B11), 22361–22374. https://doi.org/10.1029/95JB01686

Bernasconi, S. M., Daëron, M., Bergmann, K. D., Bonifacie, M., Meckler, A. N., Affek, H. P., et al. (2021). InterCarb: A community effort to improve interlaboratory standardization of the carbonate clumped isotope thermometer using carbonate standards. *Geochemistry, Geophysics, Geosystems*, *22*, e2020GC009588. https://doi.org/10.1029/2020GC009588

Blinnikov, M., Busacca, A., & Whitlock, C. (2002). Reconstruction of the late Pleistocene grassland of the Columbia basin, Washington, USA, based on phytoliths records in loess. *Palaeogeography, Palaeoclimatology, Palaeoecology*, *177*(1–2), 77–101. https://doi.org/10.1016/s0031-0182(01)00353-4

Booth, D. B., Troost, K. G., Clague, J. J., & Waitt, R. B. (2003). The Cordilleran ice sheet. *Development in Quaternary Science*, *1*, 17–43.

Braconnot, P., Harrison, S. P., Kageyama, M., Bartlein, P. J., Masson-Delmotte, V., Abe-Ouchi, A., et al. (2012). Evaluation of climate models using palaeoclimatic data. *Nature Climate Change*, *2*(6), 417–424. https://doi.org/10.1038/nclimate1456

Braconnot, P., Otto-Bliesner, B., Harrison, S., Joussaume, S., Peterchmitt, J. Y., Abe-Ouchi, A., et al. (2007). Results of PMIP2 coupled simulations of the mid-Holocene and last glacial maximum—Part 1: Experiments and large scale features. *Climate of the Past*, *3*(2), 261–277. https://doi.org/10.5194/cp-3-261-2007

Brady, E., Stevenson, S., Bailey, D., Liu, Z., Noone, D., Nusbaumer, J., et al. (2019). The connected isotopic water cycle in the Community Earth System Model version 1. *Journal of Advances in Modeling Earth Systems*, *11*, 2547–2566. https://doi.org/10.1029/2019MS001663

Breecker, D. O., Sharp, Z., & McFadden, L. (2009). Seasonal bias in the formation and stable isotopic composition of pedogenic carbonate in modern soils from central New Mexico. *GSA Bulletin*, *121*(3–4), 630–640. https://doi.org/10.1130/b26413.1

Busacca, A. J. (1989). Long Quaternary record in Eastern Washington, U.S.A., interpreted from multiple buried paleosols. *Geoderma*, *45*(2), 105–122. https://doi.org/10.1016/0016-7061(89)90045-1

Busacca, A. J., & McDonald, E. V. (1994). Regional Sedimentation of the Late Quaternary loess on the Columbia Plateau: Sediment source areas and loess distribution patterns. *Bulletin-Washington. Division of Geology and Earth Resources*, *80*, 181–203.

Cerling, T. E. (1984). The stable isotopic composition of modern soil carbonate and its relationship to climate. *Earth and Planetary Science Letters*, *71*(2), 229–240. https://doi.org/10.1016/0012-821x(84)90089-x

Clark, P. U., Dyke, A. S., Shakun, J. D., Carlson, A. E., Clark, J., Wohlfarth, B., et al. (2009). The Last Glacial Maximum. *Science*, *325*(5941), 710–714. https://doi.org/10.1126/science.1172873

Clark, P. U., & Mix, A. C. (2002). Ice sheets and sea level of the Last Glacial Maximum. *Quaternary Science Reviews*, *21*(1–3), 1–7. https://doi.org/10.1016/s0277-3791(01)00118-4

Cohmap Members. (1988). Climatic changes of the last 18,000 years: Observations and model simulations. *Science*, *241*(4869), 1043–1052.

Daeron, M., Blamart, D., Peral, M., & Affek, H. (2016). Absolute isotopic abundance ratios and the accuracy of Δ47 measurements. *Chemical Geology*, *441*, 83–96. https://doi.org/10.1016/j.chemgeo.2016.08.014

Defliese, W. F., & Tripati, A. (2020). Analytical effects on clumped isotope thermometry: Comparison of common sample set analyzed using multiple instruments, types, and standardization windows. *Rapid Communications in Mass Spectrometry*, *34*, e8666. https://doi.org/10.1002/rcm.8666

Diffenbaugh, N. S., Ashfaq, M., Shuman, B., Williams, J. W., & Bartlein, P. J. (2006). Summer aridity in the United States: Response to mid-Holocene changes in insolation and sea surface temperature. *Geophysical Research Letters*, *33*, L22712. https://doi.org/10.1029/2006GL028012

Duplessy, J. C., Labeyrie, L., & Waelbroeck, C. (2002). Constraints on the ocean oxygen isotopic enrichment between the Last Glacial Maximum and the Holocene: Paleoceanographic implications. *Quaternary Science Reviews*, *21*(1), 315–330. https://doi.org/10.1016/s0277-3791(01)00107-x

Dyke, A. S., Andrews, J., Clark, P., England, J., Miller, G., Shaw, J., & Veillette, J. (2002). The Laurentide and Innuitian ice sheets during the Last Glacial Maximum. *Quaternary Science Reviews*, *21*(1–3), 9–31. https://doi.org/10.1016/s0277-3791(01)00095-6

Eagle, R. A., Risi, C., Mitchell, J. L., Eiler, J. M., Seibt, U., Neelin, J. D., et al. (2013). High regional climate sensitivity over continental China constrained by glacial-recent changes in temperature and the hydrologic cycle. *Proceedings of the National Academy of Sciences of the United States of America*, *110*(22), 8813–8818. https://doi.org/10.1073/pnas.1213366110

Eiler, J. (2011). Paleoclimate reconstruction using carbonate clumped isotope thermometry. *Quaternary Science Reviews*, *30*(25–26), 3575–3588. https://doi.org/10.1016/j.quascirev.2011.09.001

Eiler, J. M. (2007). Clumped-isotope geochemistry—The study of naturally-occurring, multiply-substituted isotopologues. *Earth and Planetary Science Letters*, *262*(3–4), 309–327. https://doi.org/10.1016/j.epsl.2007.08.020

Epstein, S., Buchsbaum, R., Lowenstam, H. A., & Urey, H. C. (1953). Revised carbonate-water isotopic temperature scale. *Geological Society of America Bulletin*, *64*(11), 1315–1325. https://doi.org/10.1130/0016-7606(1953)64[1315:RCITS]2.0.CO;2

Fischer-Femal, B., & Bowen, G. (2021). Coupled carbon and oxygen isotope model for pedogenic carbonates. *Geochimica et Cosmochimica Acta*, *294*, 126–144. https://doi.org/10.1016/j.gca.2020.10.022

Friedman, I., & O'Neil, J. R. (1977). *Compilation of stable isotope fractionation factors of geochemical interest* (U.S. Geol. Surv. Prof. Pap. 440-KK). United States Geological Survey. https://doi.org/10.3133/pp440KK

Friedrich, T., Timmermann, A., Tigchelaar, M., Timm, O. E., & Ganopolski, A. (2016). Nonlinear climate sensitivity and it implications for future greenhouse warming. *Science Advances*, *2*(11), e1501923. https://doi.org/10.1126/sciadv.1501923

Ghosh, P., Adkins, J., Affek, H., Balta, B., Guo, W., Schauble, E. A., et al. (2006). ^{13}C–^{18}O bonds in carbonate minerals: A new kind of paleothermometer. *Geochimica et Cosmochimica Acta*, *70*(6), 1439–1456. https://doi.org/10.1016/j.gca.2005.11.014

Gildor, H., & Tziperman, E. (2001). A sea ice climate switch mechanism for the 100-kyr glacial cycles. *Journal of Geophysical Research*, *106*(C5), 9117–9133. https://doi.org/10.1029/1999JC000120

Gray, W. R., Wills, R. C., Rae, J. W., Burke, A., Ivanovic, R. F., Roberts, W. H., et al. (2020). Wind-driven evolution of the North Pacific subpolar gyre over the last deglaciation. *Geophysical Research Letters*, *47*, e2019GL086328. https://doi.org/10.1029/2019GL086328

Gregoire, L. J., Valdes, P. J., & Payne, A. J. (2015). The relative contribution of orbital forcing and greenhouse gases to the North American deglaciation. *Geophysical Research Letters*, *42*, 9970–9979. https://doi.org/10.1002/2015GL066005

Hargreaves, J. C., Annan, J. D., Ohgaito, R., Paul, A., & Abe-Ouchi, A. (2013). Skill and reliability of climate model ensembles at the Last Glacial Maximum and mid-Holocene. *Climate of the Past*, *9*(2), 811–823. https://doi.org/10.5194/cp-9-811-2013

He, F. (2011). *Simulating transient climate evolution of the last deglaciation with CCSM3 (PhD thesis)*. University of Wisconsin.

Hostetler, S. W., & Bartlein, P. J. (1999). Simulation of the potential responses of regional climate and surface processes in Western North America to a Canonical Heinrich event. *Mechanisms of Global Climate Change: American Geophysical Union Geophysical Monograph*, *12*, 313–327.

Hough, B. G., Fan, M., & Passey, B. H. (2014). Calibration of clumped isotope geothermometer in soil carbonate in Wyoming and Nebraska, USA: Implications for paleoelevation and paleoclimate reconstruction. *Earth and Planetary Science Letters*, *391*, 110–120. https://doi.org/10.1016/j.epsl.2014.01.008

Huntington, K. W., Eiler, J. M., Affek, H. P., Guo, W., Bonifacie, M., Yeung, L. Y., et al. (2009). Methods and limitations of 'clumped' CO2 isotope (Δ47) analysis by gas-source isotope ratio mass spectrometry. *Journal of Mass Spectrometry*, *44*(9), 1318–1329. https://doi.org/10.1002/jms.1614

Hurrell, J. W., Holland, M. M., Gent, P. R., Ghan, S., Kay, J. E., Kushner, P. J., et al. (2013). The community Earth system model: A framework for collaborative research. *Bulletin of the American Meteorological Society*, *94*(9), 1339–1360. https://doi.org/10.1175/bams-d-12-00121.1

John, C. M., & Bowen, D. (2016). Community software for challenging isotope analysis: First applications of 'Easotope' to clumped isotopes. *Rapid Communications in Mass Spectrometry*, *30*(21), 2285–2300. https://doi.org/10.1002/rcm.7720

Kageyama, M., Braconnot, P., Harrison, S. P., Haywood, A. M., Jungclaus, J. H., Otto-Bliesner, B. L., et al. (2018a). The PMIP4 contribution to CMIP6 – Part 1: Overview and over-arching analysis plan. *Geoscientific Model Development*, *11*(3), 1033–1057. https://doi.org/10.5194/gmd-11-1033-2018

Kageyama, M., Braconnot, P., Harrison, S. P., Haywood, A. M., Jungclaus, J. H., Otto-Bliesner, B. L., et al. (2018b). PMIP4-CMIP6: The contribution of the Paleoclimate Modeling Intercomparison Project to CMIP6. *Geoscientific Model Development Discussions*, *11*(3), 1033–1057. https://doi.org/10.5194/gmd-11-1033-2018

Kageyama, M., Harrison, S. P., Kapsch, M. L., Lofverstrom, M., Lora, J. M., Mikolajewicz, U., et al. (2021). The PMIP4 Last Glacial Maximum experiments: Preliminary results and comparison with the PMIP3 simulations. *Climate of the Past*, *17*(3), 1065–1089. https://doi.org/10.5194/cp-17-1065-2021

Kaufman, D. S., Ager, T. A., Anderson, N. J., Anderson, P. M., Andrews, J. T., Bartlein, P. J., et al. (2004). Holocene thermal maximum in the Western Arctic (0–180 W). *Quaternary Science Reviews*, *23*(5–6), 529–560. https://doi.org/10.1016/j.quascirev.2003.09.007

Kelson, J., Huntington, K. W., Breecker, D. O., Burgener, L. K., Gallagher, T. M., Hoke, G. D., & Petersen, S. V. (2020). A proxy for all seasons? A synthesis of clumped isotope data from Holocene soil carbonates. *Quaternary Science Reviews*, *234*, 106259. https://doi.org/10.1016/j.quascirev.2020.106259

Kennedy, K. E., Froese, D., Zazula, G., & Lauriol, B. (2010). Last Glacial Maximum age for the northwest Laurentide maximum from the Eagle River spillway and delta complex, northern Yukon. *Quaternary Science Reviews*, *29*(9–10), 1288–1300. https://doi.org/10.1016/j.quascirev.2010.02.015

Kim, S., & O'Neil, J. R. (1997). Equilibrium and nonequilibrium oxygen isotope effects in synthetic carbonates. *Geochimica et Cosmochimica Acta*, *61*(16), 3461–3475. https://doi.org/10.1016/s0016-7037(97)00169-5

Lacelle, D., Lauriol, B., Zazula, G., Ghaleb, B., Utting, N., & Clark, I. D. (2013). Timing of advance and basal condition of the Laurentide Ice Sheet during the last glacial maximum in the Richardson Mountains, NWT. *Quaternary Research*, *80*(2), 274–283. https://doi.org/10.1016/j.yqres.2013.06.001

Lambeck, K., Purcell, A., Zhao, J., & Svensson, N. O. (2010). The Scandinavian ice sheet: From MIS 4 to the end of the last glacial maximum. *Boreas*, *39*(2), 410–435. https://doi.org/10.1111/j.1502-3885.2010.00140.x

Lechler, A. R., Huntington, K. W., Breecker, D. O., Sweeney, M. R., & Schauer, A. J. (2018). Loess-paleosol carbonate clumped isotope record of late Pleistocene-Holocene climate change in the Palouse region, Washington State, USA. *Quaternary Research*, *90*(2), 1–17. https://doi.org/10.1017/qua.2018.47

LeGrande, A. N., & Schmidt, G. A. (2006). Global gridded data set of the oxygen isotopic composition in seawater. *Geophysical Research Letters*, *33*, L12604. https://doi.org/10.1029/2006GL026011

LeGrande, A. N., & Schmidt, G. A. (2008). Ensemble, water isotope–enabled, coupled general circulation modeling insights into the 8.2 ka event. *Paleoceanography*, *23*, PA3207. https://doi.org/10.1029/2008PA001610

Li, G., Chen, J., & Chen, Y. (2013). Primary and secondary carbonate in Chinese loess discriminated by trace element composition. *Geochimica et Cosmochimica Acta*, *103*, 26–35. https://doi.org/10.1016/j.gca.2012.10.049

Lisiecki, L. E., & Raymo, M. E. (2005). A Pliocene-Pleistocene stack of 57 globally distributed benthic δ18O records. *Paleoceanography*, *20*, PA1003. https://doi.org/10.1029/2004PA001071

Lisiecki, L. E., & Stern, J. V. (2016). Regional and global benthic δ18O stack for the last glacial cycle. *American Geophysical Union*, *31*(10), 1368–1398.
Liu, Z., Otto-Bliesner, B. L., He, F., Brady, E. C., Tomas, R., Clark, P. U., et al. (2009). Transient Simulation of Las Deglaciation with a New Mechanism for BØlling-AllerØd Warming. *Science*, *325*(5938), 310–314. https://doi.org/10.1126/science.1171041
Lopez-Maldonado, R., Bateman, J. B., Ellis, A., Bader, N. E., Ramirez, P., Arnold, A., et al. (2022). *NOAA/WDS Paleoclimatology—Clumped isotope measurements and temperature estimates from Palouse Loess, Washington from 34000 to 9000 BP*. NOAA National Centers for Environmental Information. https://doi.org/10.25921/r09x-m706
Lora, J. M., Mitchell, J. L., Risi, C., & Tripati, A. E. (2017). North Pacific atmospheric rivers and their influence on Western North America at the Last Glacial Maximum. *Geophysical Research Letters*, *44*, 1051–1059. https://doi.org/10.1002/2016GL071541
Lora, J. M., Mitchell, J. L., & Tripati, A. E. (2016). Abrupt reorganization of the North Pacific and Western North American climate during the last deglaciation. *Geophysical Research Letters*, *43*, 11796–11804. https://doi.org/10.1002/2016GL071244
Lucarelli, J. K., Carroll, H. M., Elliott, B. M., & Eagle, R. (2021). Equilibrated gas and carbonate standard-derived paired clumped isotope (Δ47 and Δ48) values on the absolute reference frame. *Geochemistry, Geophysics, Geosystems*, *23*, e2022GC010458. https://doi.org/10.1029/2022GC010458
Lyle, M., Heusser, L., Ravelo, C., Yamamoto, M., Barron, J., Diffenbaugh, N. S., et al. (2012). Out of the tropics: The Pacific, Great Basins Lakes, and late Pleistocene water cycle in the Western United States. *Science*, *337*(6102), 1629–1633. https://doi.org/10.1126/science.1218390
Manabe, S., & Broccoli, A. J. (1985). The influence of continental ice sheets on the climate of the Ice Age. *Journal of Geophysical Research*, *90*(D1), 2167–2190. https://doi.org/10.1029/JD090id01p02167
Marcott, S. A., Shakun, J. D., Clark, P. U., & Mix, A. C. (2013). A reconstruction of regional and global temperature for the past 11,300 years. *Science*, *339*(6124), 1198–1201. https://doi.org/10.1126/science.1228026
Martinson, D. G., Pisias, N. G., Hays, J. D., Imbrie, J., Moore, T. C., & Shackleton, N. J. (1987). Age dating and the orbital theory of the ice ages: Development of a high resolution 0 to 300,000-year chronostratigraphy. *Quaternary Research*, *27*, 1–29. https://doi.org/10.1016/0033-5894(87)90046-9
Mayewski, P. A., Rohling, E. E., Curt Stager, J., Karlen, W., Maasch, K. A., Meeker, L. D., et al. (2004). Holocene climate variability. *Quaternary Research*, *62*(3), 243–255. https://doi.org/10.1016/j.yqres.2004.07.001
McCrea, J. M. (1950). On the isotopic chemistry of carbonates and a paleotemperature scale. *The Journal of Chemical Physics*, *18*(6), 849–857. https://doi.org/10.1063/1.1747785
McDonald, E. V., & Busacca, A. J. (1992). Late quaternary stratigraphy of loess in the Channeled Scabland and Palouse regions of Washington State. *Quaternary Research*, *38*(2), 141–156. https://doi.org/10.1016/0033-5894(92)90052-k
McDonald, E. V., Sweeney, M. R., & Busacca, A. J. (2012). Glacial outburst floods and loess sedimentation documented during Oxygen Isotope Stage 4 on the Columbia Plateau, Washington State. *Quaternary Science Reviews*, *45*, 18–30. https://doi.org/10.1016/j.quascirev.2012.03.016
Meltzer, D. J., & Holliday, V. T. (2010). Would North America Paleoindians have noticed Younger Dryas Age Climate Change? *Journal of World Prehistory*, *23*, 1–41. https://doi.org/10.1007/s10963-009-9032-4
Mix, A. C., Bard, E., & Schneider, R. (2001). Environmental processes of the ice age: Land, oceans, glaciers (EPILOG). *Quaternary Science Reviews*, *20*(4), 627–657. https://doi.org/10.1016/s0277-3791(00)00145-1
Munro, J. S., & Laabs, B. J. C. (2013). Temporal correspondence between pluvial lake highstands in the southwestern US and Heinrich Event 1. *Journal of Quaternary Science*, *28*, 49–58. https://doi.org/10.1002/jqs.2586
Murton, J. B., Frechen, M., & Maddy, D. (2007). Luminescence dating of mid-to Late Wisconsinian aeolian sand as a constraint on the last advance of the Laurentide Ice Sheet across the Tuktoyaktuk coastlands, Western Arctic Canada. *Canadian Journal of Earth Sciences*, *44*(6), 857–869. https://doi.org/10.1139/e07-015
Nusbaumer, J., Wong, T. E., Bardeen, C., & Noone, D. (2017). Evaluating hydrological processes in the Community Atmosphere Model Version 5 (CAM5) using stable isotope ratios of water. *Journal of Advances in Modeling Earth Systems*, *9*(2), 949–977. https://doi.org/10.1002/2016ms000839
Osman, M. B., Tierney, J. E., Zhu, J., Tardif, R., Hakim, G. J., King, J., & Poulsen, C. J. (2021). Globally resolved surface temperatures since the Last Glacial Maximum. *Nature*, *599*(7884), 239–244. https://doi.org/10.1038/s41586-021-03984-4
Passey, B. H., Levin, N. E., Cerling, T. E., Brown, F. H., & Eiler, J. M. (2010). High-temperature environments of human evolution in East Africa based on bond ordering in paleosol carbonates. *Proceedings of the National Academy of Sciences of the United States of America*, *107*(25), 11245–11249. https://doi.org/10.1073/pnas.1001824107
Peltier, W. R., Argus, D. F., & Drummond, R. (2015). Space geodesy constrains ice age terminal deglaciation: The global ICE-6G_C (VM5a) model. *Journal of Geophysical Research: Solid Earth*, *120*, 450–487. https://doi.org/10.1002/2014JB011176
Peters, N. A., Huntington, K. W., & Hoke, G. D. (2012). Hot or not? Impact of seasonally variable soil carbonate formation on paleotemperature and O-isotope records from clumped isotope thermometry. *Earth and Planetary Science Letters*, *361*, 208–218. https://doi.org/10.1016/j.epsl.2012.10.024
PRISM Climate Group, Oregon State University. (2021). Data created. Retrieved from https://prism.oregonstate.edu
Quade, J., Eiler, J., Daeron, M., & Achyuthan, H. (2013). The clumped isotope geothermometer in soil and paleosol carbonate. *Geochimica et Cosmochimica Acta*, *105*, 92–107. https://doi.org/10.1016/j.gca.2012.11.031
Raynaud, D., Jouzel, J., Barnola, J. M., Chappellaz, J., Delmas, R. J., & Lorius, C. (1993). The ice record of greenhouse gases. *Science*, *259*(5097), 926–933. https://doi.org/10.1126/science.259.5097.926
Reheis, M. C., Adams, K. D., Oviatt, C. G., & Bacon, S. N. (2014). Pluvial lakes in the Great Basin of Western United States—A view from the outcrop. *Quaternary Science Reviews*, *97*, 33–57. https://doi.org/10.1016/j.quascirev.2014.04.012
Richardson, C. A., McDonald, E., & Busacca, A. (1997). Luminescence dating of loess from the northwest United States. *Quaternary Science Reviews*, *16*(3–5), 403–415. https://doi.org/10.1016/s0277-3791(96)00111-4
Richardson, C. A., McDonald, E. V., Busacca, A. J., & Livingstone, E. I. (1999). A luminescence chronology for loess deposition in Washington state and Oregon, USA. *Zeitschrift fur Geomorphologie Supplementband*, *116*, 77–95.
Roberts, C. D., LeGrande, A. N., & Tripati, A. K. (2011). Sensitivity of seawater oxygen isotopes to climatic and tectonic boundary conditions in an early Paleogene simulation with GISS ModelE-R. *Paleoceanography*, *26*. https://doi.org/10.1029/2010PA002025
Santi, L. M., Arnold, A. J., Ibarra, D. E., Whicker, C. A., Mering, J. A., Lomarda, R. B., et al. (2020). Clumped isotope constraints on changes in latest Pleistocene hydroclimate in the northwestern Great Basin: Lake Surprise, California. *GSA Bulletin*, *132*(11–12), 2669–2683. https://doi.org/10.1130/b35484.1
Shakun, J. D., Clark, P. U., He, F., Marcott, S. A., Mix, A. C., Liu, Z., et al. (2012). Global warming preceded by increasing carbon dioxide concentrations during the last deglaciation. *Nature*, *484*(7392), 49–55. https://doi.org/10.1038/nature10915

Sheldon, N. D., & Tabor, N. J. (2009). Quantitative paleoenvironmental and paleoclimatic reconstruction using paleosols. *Earth-Science Reviews*, *95*(1–2), 1–52. https://doi.org/10.1016/j.earscirev.2009.03.004

Skinner, C. B., Lora, J. M., Payne, A. E., & Poulsen, C. J. (2020). Atmospheric river changes shaped mid-latitude hydroclimate since the mid-Holocene. *Earth and Planetary Science Letters*, *541*, 116293. https://doi.org/10.1016/j.epsl.2020.116293

Spencer, P. K., & Knapp, A. N. (2010). New stratigraphic markers in the late Pleistocene Palouse loess: Novel fossil gastropods, absolute age constraints and non-aeolian facies. *Sedimentology*, *57*(1), 41–52. https://doi.org/10.1111/j.1365-3091.2009.01085.x

Stevenson, B. A. (1997). *Stable carbon and oxygen isotopes in soils and paleosols of the Palouse Loess, Eastern Washington State: Modern relationships and applications for paleoclimatic reconstruction* (Doctoral dissertation). Colorado State University.

Stokes, C. R. (2017). Deglaciation of the Laurentide ice sheet from the last glacial maximum. *Geophysical Research Letters*, *43*, 377–428. https://doi.org/10.18172/cig.3237

Sweeney, M. R., Busacca, A. J., & Gaylord, D. R. (2005). Topographic and climatic influences on accelerated loess accumulation since the last glacial maximum in the Palouse, Pacific Northwest, USA. *Quaternary Research*, *63*(3), 261–273. https://doi.org/10.1016/j.yqres.2005.02.001

Sweeney, M. R., Busacca, A. J., Richardson, C., Blinnikov, M., & McDonald, E. (2004). Glacial anticyclone recorded in Palouse loess of northwestern United States. *Geology*, *32*(8), 705–708. https://doi.org/10.1130/g20584.1

Sweeney, M. R., Gaylord, D. R., & Busacca, A. J. (2007). Evolution of Eureka Flat: A dust-producing engine of the Palouse loess, USA. *Quaternary International*, *162*, 76–96. https://doi.org/10.1016/j.quaint.2006.10.034

Tabor, C. (2021). Data used in paleoclimate changes in the Pacific Northwest over the past 36,000 years from clumped isotope measurements and isotope-enabled model analysis [Dataset]. Zenodo. https://doi.org/10.5281/zenodo.5585291

Tabor, C., Lofverstrom, M., Oster, J., Wortham, B., de Wet, C., Montanez, I., et al. (2021). A mechanistic understanding of oxygen isotopic changes in the Western United States at the Last Glacial Maximum. *Quaternary Science Reviews*, *274*, 107255. https://doi.org/10.1016/j.quascirev.2021.107255

Takeuchi, A., Goodwin, A. J., Moravec, B. G., Larson, P. B., & Keller, C. K. (2009). Isotopic evidence for temporal variation in proportion of seasonal precipitation since the last glacial time in the inland Pacific Northwest of the USA. *Quaternary Research*, *72*(2), 198–206. https://doi.org/10.1016/j.yqres.2009.06.001

Tarasov, L., Dyke, A. S., Neal, R. M., & Peltier, W. (2012). A data-calibrated distribution of deglacial chronologies for the North American ice complex from glaciological modeling. *Earth and Planetary Science Letters*, *315–316*, 30–40. https://doi.org/10.1016/j.epsl.2011.09.010

Tierney, J. E., Zhu, J., King, J., Malevich, S. B., Hakim, G. J., & Poulsen, C. J. (2020). Glacial cooling and climate sensitivity revisited. *Nature*, *584*(7822), 569–573. https://doi.org/10.1038/s41586-020-2617-x

Tripati, A. K., Hill, P. S., Eagle, R. A., Mosenfelder, J. L., Tang, J., Schauble, E. A., et al. (2015). Beyond temperature: Clumped isotope signatures in dissolved inorganic carbon species and the influence of solution chemistry on carbonate mineral composition. *Geochimica et Cosmochimica Acta*, *166*, 344–371. https://doi.org/10.1016/j.gca.2015.06.021

Ullman, D. J., Carlson, A. E., Anslow, F. S., LeGrande, A. N., & Licciardi, J. M. (2015). Laurentide ice-sheet instability during the last deglaciation. *Nature Geosience*, *8*(7), 534–537. https://doi.org/10.1038/ngeo2463

Ullman, D. J., Carlson, A. E., LeGrande, A. N., Anslow, F. S., Moore, A. K., Caffee, M., et al. (2015). Southern Laurentide ice-sheet retreat synchronous with rising boreal summer insolation. *Geology*, *43*(1), 23–26. https://doi.org/10.1130/g36179.1

Upadhyay, D., Lucarelli, J., Arnold, A., Flores, R., Bricker, H., Ulrich, R. N., et al. (2021). Carbonate clumped isotope analysis (Δ47) of 21 carbonate standards determined via gas-source isotope-ratio mass spectrometry on four instrumental configurations using carbonate-based standardization and multiyear data sets. *Rapid Communications in Mass Spectrometry*, *35*(17), e9143. https://doi.org/10.1002/rcm.9143

Wagner, J. D. M., Cole, J. E., Beck, J. W., Patchett, P. J., Henderson, G. M., & Barnett, H. R. (2010). Moisture variability in the southwestern United States linked to abrupt glacial climate change. *Nature Geoscience*, *3*(2), 110–113. https://doi.org/10.1038/ngeo707

Weaver, P. P., Carter, L., & Neil, H. L. (1998). Response of surface water masses and circulation to late Quaternary climate change east of New Zealand. *Paleoceanography*, *13*(1), 70–83. https://doi.org/10.1029/97PA02982

Whitlock, C. (1992). Vegetational and climatic history of the Pacific Northwest during the last 20,000 years: Implications for understanding present-day biodiversity. *Northwest Environmental Journal*, *8*, 5–28.

Whitlock, C., & Bartlein, P. J. (1997). Vegetation and climate change in northwest America during the past 125 kyr. *Nature*, *388*(6637), 57–61. https://doi.org/10.1038/40380

Whitlock, C., Sarna-Wojcicki, A. M., Bartlein, P. J., & Nickmann, R. J. (2000). Environmental history and tephrostratigraphy at Carp Lake, southwestern Columbia Basin. *Palaeogeography, Palaeoclimatology, Palaeoecology*, *155*, 7–29. https://doi.org/10.1016/s0031-0182(99)00092-9

Wong, T. E., Nusbaumer, J., & Noone, D. C. (2017). Evaluation of modeled land-atmosphere exchanges with a comprehensive water isotope fractionation scheme in version 4 of the Community Land Model. *Journal of Advances in Modeling Earth Systems*, *9*, 978–1001. https://doi.org/10.1002/2016MS000842

Yanase, W., & Abe-Ouchi, A. (2010). A numerical study on the atmospheric circulation over the midlatitude North Pacific during the last glacial maximum. *Journal of Climate*, *23*(1), 135–151. https://doi.org/10.1175/2009JCLI3148.1

Zhu, J., Liu, Z., Brady, E., Otto-Bliesner, B., Zhang, J., Noone, D., et al. (2017). Reduced ENSO Variability at the LGM revealed by an isotope-enabled Earth System Model. *Geophysical Research Letters*, *44*, 6984–6992. https://doi.org/10.1002/2017GL073406

References From the Supporting Information

Barta, G. (2011). Secondary carbonates in loess-paleosol sequences: A general review. *Central European Journal of Geosciences*, *3*(2), 129–146. https://doi.org/10.2478/s13533-011-0013-7

Dennis, K. J., Affek, H. P., Passey, B. H., Schrag, D. P., & Eiler, J. M. (2011). Defining an absolute reference frame for 'clumped' isotope studies of CO_2. *Geochimica et Cosmochimica Acta*, *75*(22), 7117–7131. https://doi.org/10.1016/j.gca.2011.09.025

Dickson, J. A. D. (1966). Carbonate identification and Genesis as revealed by staining. *Sedimentary Petrology*, *36*(2), 491–505.

Durand, N., Monger, H. C., & Canti, M. G., (2010). *Interpretation of micromorphological features of soils and regolith* (pp. 149–194). Elsevier.

Lopez-Maldonado, R. (2017). *Carbonate clumped isotope reconstruction of temperatures and water 18O/16O ratios from Last glacial maximum and holocene climatic optimum age calcic paleosols in the palouse loess (Washington, USA)* (MS thesis, p. 108). California State University.

Wang, Z., Schauble, E. A., & Eiler, J. M. (2004). Equilibrium thermodynamics of multiply-substituted isotopologues of molecular gases. *Geochimica et Cosmochimica Acta*, *23*, 4779–4797. https://doi.org/10.1016/j.gca.2004.05.039

Zamanian, K., Pustovoytov, K., & Kuzyakov, Y. (2016). Pedogenic carbonates: Forms and formation processes. *Earth-Science Reviews*, *157*, 1–17. https://doi.org/10.1016/j.earscirev.2016.03.003

Zhang, J., Liu, Z., Brady, E. C., Oppo, D. W., Clark, P. U., Jahn, A., et al. (2017). Asynchronous warming and δ18O evolution of deep Atlantic water masses during the last deglaciation. *Proceedings of the National Academy of Sciences of the United States of America*, *114*(42), 11075–11080. https://doi.org/10.1073/pnas.1704512114